Electronic Supplementary Information

Sequential Separation-driven Solar Methane Reforming for H_2 Derivation under Mild Conditions

Yunyi Ling[ab], Hongsheng Wang[a], Mingkai Liu[ab], Bin Wang[ac], Shuang Li[d], Xuancan Zhu[d], Yixiang Shi[d], Hongde Xia[a], Ke Guo[ae], Yong Hao[*ab], Hongguang Jin[ab]

[a]Institute of Engineering Thermophysics, Chinese Academy of Sciences, Beijing 100190, PR China.

[b]University of Chinese Academy of Sciences, Beijing 100049, PR China.

[c]Wu Zhonghua College, North China Electric Power University, Beijing 102206, PR China.

[d]Key Laboratory for Thermal Science and Power Engineering of Ministry of Education, Department of Energy and Power Engineering, Tsinghua University, Beijing 100084, PR China.

[e]Department of Thermal Science and Energy Engineering, University of Science and Technology of China, Hefei 230027, PR China

*Corresponding author. Email: haoyong@iet.cn.

This PDF file includes:

Materials and Methods

Material preparation

Commercial Ni (40 wt%) / MgO-Al_2O_3 catalyst was supplied by Liaoning Haitai Company. The bulk density and specific surface area of Ni/MgO-Al_2O_3 catalyst were 2.21 g mL^{-1} and 80 m^2 g^{-1}, respectively. Characterization of the catalyst is shown in Fig.s S5 to S7.

The sorbent composite (20 wt% K_2CO_3 promoted γ-alumina /$Mg_6Al_2CO_3(OH)_{16}$ hydrotalcite) was made by PURAL MG63 from SASOL Germany GmbH, alumina gel and potassium carbonate powder as starting materials. It was fabricated by the authors following specific extruding steps. The main active component of the sorbent was K-promoted MgAl-layered double oxides, while K-promoted γ-alumina was adherent in extruding process. Solution impregnation method was used to promote the hydrotalcite. The specific surface area of the adsorbent was 42.6 m^2 g^{-1}, and the adsorption capacity was 0.6 mmol g^{-1} at ambient temperature and pressure. Characterization of the hydrotalcite sorbent is shown in Fig.s S9 to S10.

Reactor setup

The reactor was placed inside an electric furnace (SKGL-1200C, Shanghai Jujing Precision Instrument Manufacturing Co., Ltd.). Digital mass flow controllers (SevenStar CS200A, Beijing Sevenstar Flow Co., LTD.) supplied Ar and CH_4 to the reactor, in which Ar was used as the internal standard gas of mass spectrometry for quantitative measurement of effluent gas. Deionized water was injected by a constant flow pump (Elite P230II), after which it was vaporized and heated to 200°C by an in-house steam generator. The effluent gas composition was analyzed using a mass spectrometer (Pfeiffer Omnistar GSD 320) with equivalent characteristic spectrum analysis (ECSA®) method (detailed below). H_2 was separated by the Pd-Ag membrane of the reactor with a vacuum pump (WELCH MPC 601 T ef, Gardner Denver Thomas, Inc.) at selected vacuum levels (vacuum control box: WELCH VCB 521 ef). The real-time mass flow rate of H_2 produced was measured by a digital mass flow controller as introduced above, which was connected between the Pd-Ag membrane and the vacuum pump. The digital mass flow controller was used as a mass flow meter by setting the valve position to be normally open.

The reactor was integrated with a parabolic trough solar collector with a reflecting mirror (2.55 m in aperture, 1.5 m in length) and a steel receiver tube (38 mm in inner diameter, 40 mm in outer diameter, with evacuated glass envelop on the exterior). Five K-type thermocouples (OMEGA TJ80-CAXL-040U-20)

were placed inside the stainless-steel mesh to monitor temperature distribution along axial direction (Table S13). The Pd-Ag membrane tube was wrapped with the stainless-steel mesh (38 mm in outer diameter). The reflectivity of the parabolic solar reflector was 95 ± 2%. The absorptivity and emissivity of the absorber with selective absorbing coating was 95 ± 2% and 10 ± 2%, respectively. Solar irradiation was provided by an in-house universal solar simulator that mimics natural sunlight with excellent collimation and uniformity.[1]

The selected irradiation measurement points were within the rectangular range of 1.0 m^2 formed by the reactor tube length (0.38 m) and the aperture size of solar trough mirror (2.55 m). The measurement results are shown in Table S3. The temperature distribution in the reaction bed of solar collector tube was also measured. As shown in Fig. S11, five thermocouples were arranged along the circumferential direction, and the temperature distribution within the solar collector tube can be measured by extending the thermocouples into different depths (i.e., -0.2 m, 0 m and 0.2 m) of the catalyst bed and sorbent bed. The measured temperature results are shown in Table S4. The circumferential temperature difference of solar collector tube reactor is less than 8.7ºC.

Except for the difference in heating mode, the electric furnace reactor and the solar reactor shared the same design, including the size of the Pd-Ag membrane, the filling method and quantity of catalyst and sorbent (Fig. S12). A Pd-Ag alloy membrane of 3 μm in thickness, supported on a porous ceramic tube (7 mm in inner diameter, 380 mm in length) was pumped from the interior at designated vacuum levels for H_2 separation. A concentric stainless-steel mesh (30 mm in inner diameter) housed the bed of steam methane reforming (SMR) catalyst (5.8 g for each set, 1.9-2.4 mm in diameter, 8 mm in bed height) and CO_2 sorbent (21.7 g for each set, 0.8-1.9 mm in diameter, 55 mm in bed height), which were arranged in an alternating fashion. A total of 6 sets of catalyst / absorbent combination was used (bed heights of 8 mm / 55 mm, respectively).

Experimental procedure

Gas-tightness test of the Pd-Ag membrane was performed before the reaction. Gaseous mixture of Ar, CH_4, and CO_2 was introduced into the reactor. The pressure of the gaseous mixture was maintained at 2×10^5 Pa on the external side of the Pd-Ag membrane (i.e., within the annular space between the membrane tube and stainless-steel enclosure of the reactor). The internal side of the Pd-Ag membrane (i.e., the permeate

side during normal operation of the reactor) was connected to a tube, the outlet of which was submerged under water at ambient pressure. If no bubbles were observed for 10 minutes, the Pd-Ag membrane was regarded as gastight to gases other than H_2.

Before the SMR reaction, reduction of SMR catalyst and desorption of hydrotalcite were carried out, in order to convert nickel oxide to nickel and to release adsorbed CO_2, respectively. During the catalyst reduction, hydrogen was introduced into the reactor at a flow rate of 200 mL min^{-1} (standard temperature and pressure, STP) for 2 h at 300°C and 10^5 Pa; then the temperature was increased to 400°C (heating rate of 50°C min^{-1}) and the same hydrogen flow was maintained for 2 h until the catalyst was fully reduced, for which CH_4 in the effluent decreased to below 0.1 mol%. During the desorption process of hydrotalcite, helium was introduced into the reactor at a flow rate of 200 mL min^{-1} (STP) for 4 h to fully desorb the hydrotalcite at 400°C and 10^5 Pa, for which CO_2 in the effluent decreased to below 0.1 mol%.

The sequential separation-driven SMR was carried out under the conditions of reaction temperature of 250-425°C, hydrogen separation pressure of 2000-8000 Pa, methane flow rate of 60-120 mL min^{-1} (STP), and steam-methane-ratio of 4. In each reaction-desorption cycle, the hydrogen produced was separated by the Pd-Ag membrane, and the carbon dioxide produced was adsorbed by the hydrotalcite. In the desorption step, hydrotalcite was purged by helium at 1000 mL min^{-1} (STP). A typical experimental condition for sequential separation-driven SMR is shown in Table S1.

Baseline experiment

The baseline of the reactor was first measured without loading catalyst or adsorbent. The baseline experiment was carried out at 400°C and 10^5 Pa. During the experiment, gaseous reactants were introduced into the reactor at the same flow rates as those in experiments with sequential separation of products. Steam and Ar were introduced at fixed flow rates (steam at 100 mL min^{-1} and Ar at 100 mL min^{-1}, STP), and methane was introduced into the reactor with step changes in flow rate (0-60-80-100-120-100-80-60-0 mL min^{-1}, STP).

Components of the tail gas were analyzed by the mass spectrometer. Fig. S13 shows the comparison between the set methane flow rate and the measured methane flow rate in the tail gas. Results show that the measured value was equal to the set value when the flow rate is stable, which proved that in the absence of catalyst, no methane reforming reaction occurred in the reactor.

Reference experiment (Ni catalyst fixed bed & hydrotalcite fixed bed)

Fixed bed experiments were carried out with Ni or hydrotalcite sorbent independently as references (Table S14). In the experiments, methane conversion rate was measured with the same gas hourly space velocity (GHSV) as that in sequential separation-driven SMR reaction, while only one material, i.e., Ni catalyst or hydrotalcite, is loaded in the reactor at a time. Steam was introduced at a steam-to-methane ratio of 4.

The tail gas components were analyzed by the mass spectrometer, and the conversion rate of methane is shown in Fig. S14. Results show that methane did not react with steam when only hydrotalcite was loaded in the reactor. The methane conversion rates were close to the thermodynamic equilibrium conversion rates when only nickel catalyst was loaded in the reactor.

Long-term durability experiment

Sequential separation-driven SMR reaction includes a reaction step, a dwelling step and a purge step, and the three steps constitute a cycle. In the long-term durability experiment, a total of 6000 cycles were performed. The specific experimental conditions are shown in Table S2.

During the reaction step, the mixture of methane and argon was introduced at a controlled flow rate into the reactor for 1 min. Then the mixture flow was stopped, and the reactor dwelled for one more minute. During the purging step, helium was introduced into reactor, and the purge time was 2 min. Steam was continuously fed into the reactor, and the ratio of total steam to methane was 4. Steam was fed continuously to avoid methane cracking and subsequent carbon deposition on catalysts in the absence of water.

Noble metal catalyst experiment for SMR

Sequential separation-driven SMR experiment with noble metal catalyst (Ru (1 wt%) / MgO-Al_2O_3 catalyst supplied by Liaoning Haitai Company) was carried out under reaction temperature of 250-400°C, hydrogen separation pressure of 2000 Pa, methane flow rate of 10 mL min^{-1} (STP), and steam-to-methane ratio of 4:1. In each reaction-desorption cycle, the hydrogen produced was separated by the Pd-Ag membrane, and the carbon dioxide produced was adsorbed by the hydrotalcite. The desorption processes used helium purging at 1000 mL min^{-1} (STP). The parameters of catalyst and hydrotalcite are shown in Table S15. Experimental condition for noble metal catalyst (1 wt % Ru) experiment is shown in Table S16.

The experimental results are shown in Fig. S1. The results show that the methane conversion rate can reach 99% at 350°C and 1 bar with steam-to-methane ratio of 4:1.

Regeneration of sorbent

Regeneration of hydrotalcite sorbent was realized by a pressure swing resulting from helium sweeping to lower CO_2 partial pressure under each reaction temperature isothermally and 1 bar total pressure. Adsorption-desorption cyclic experiment of the hydrotalcite sorbent was performed by thermogravimetry (TG) measurement: 3 mg of the sorbent sample was heated to 400°C in an inert gas atmosphere (100 mL min^{-1}) in the TG, and the temperature was maintained for 6 h to ensure full calcination. The adsorption-desorption cycle procedure (Table S17) is described as follows:

(1) CO_2 adsorption: CO_2 (40 mL min^{-1}) + He (60 mL min^{-1}) for 30 min.

(2) CO_2 desorption: He (100 mL min^{-1}) for 30 min.

The thermogravimetric curves at different temperatures are shown in Fig. S3A.

Fig. S3B shows the regeneration heat of different sorbents. Hydrotalcite is a weakly bonded chemical adsorbent with the regeneration heat of about 60 kJ mol^{-1}, and its regeneration difficulty lies between activated carbon and calcium oxide. In the cyclic experiment, only part of the capacity of hydrotalcite is utilized (shown in the purple part of the figure). The corresponding regeneration heat of this part is about 20 kJ mol^{-1}.

For comparison, regeneration of $CaCO_3$ is much more difficult. Fig. S3C shows the relationship between the equilibrium CO_2 equivalent partial pressure and temperature required for $CaCO_3$ decomposition. Assuming that when $CaCO_3$ is completely decomposed, the released CO_2 gas pressure is 10^5 Pa and reaction is carried out in a constant volume system. The CO_2 pressure (defined as CO_2 equivalent partial pressure) changes with decomposition temperature, as shown in Fig. S3C. Extremely high temperature (>1000°C) is needed for complete regeneration of $CaCO_3$ by thermodynamics.

Simulation model

The model was implemented in gPROMS® [2] in a 1D model setting with fully coupled equations for fluid motion, energy transport, mass transport, and chemical reactions. The following sections briefly describe the implementation.

Fluid motion

The catalyst and hydrotalcite sorbent can be approximated as a homogeneous packed beds with mm-size pores for the convenience of simulation (Table S18). The governing equations are given as follows:

The pressure drop along the bed is described by the Ergun equation (Eq. S1). The steady-state momentum equation of the reactants inside the cavity reactor is described by:[3]

$$-\frac{\partial p}{\partial z}=\frac{150\mu(1-\varepsilon_{\mathrm{b}})^{2}}{\varepsilon_{\mathrm{b}}^{3}D_{\mathrm{p}}^{2}}v+1.75\frac{(1-\varepsilon_{\mathrm{b}})\rho_{\mathrm{g}}}{\varepsilon_{\mathrm{b}}^{3}D_{\mathrm{p}}}v|v| \tag{S1}$$

where ε_{b} is the porosity of the catalyst bed or hydrotalcite bed; p, v and μ are the pressure, gas velocity and the dynamic viscosity of the reactants, respectively; ρ_{g} is the gas density; D_{p} represents characteristic diameter of the catalyst or hydrotalcite sorbent particle.

Mass transport

With the assumption of surface adsorption-controlled kinetics, axially dispersed plug flow, no radial mass/velocity gradients, and isothermal operation condition, the mass balance equation is given as:

$$\varepsilon_{\mathrm{b}}\frac{\partial C_{i}}{\partial t}=\varepsilon_{\mathrm{b}}\frac{\partial}{\partial z}\left(D_{\mathrm{ax},i}C_{T}\frac{\partial x_{i}}{\partial z}\right)-\frac{\partial}{\partial z}(vC_{i})-(1-\varepsilon_{\mathrm{b}})\dot{C}_{\mathrm{transfer},i} \tag{S2}$$

$$\dot{C}_{\mathrm{transfer},i}=sto_{\mathrm{a},i}\times rate_{\mathrm{a}}+sto_{\mathrm{c},i}\times R_{i}+sto_{\mathrm{h},i}\times A_{\mathrm{mem}}\times J_{\mathrm{H_2}} \tag{S3}$$

where $sto_{\mathrm{a},i}$ is 0 except +1 for CO_2, $sto_{\mathrm{c},i}$ is +1 for reaction rate R_i, and $sto_{\mathrm{h},i}$ is 0 except +1 for H_2. A_{mem} and $J_{\mathrm{H_2}}$ are the membrane area and hydrogen flux, respectively. Reaction rate of methane steam reforming is given as:

$$R_{i}=\sum_{j=1}^{3}\sigma_{ij}N_{i}r_{j} \tag{S4}$$

where the subscript *i* represents gas-phase species *i* (*i*= 1, 2, 3, 4 and 5 corresponding to the species of CH_4, H_2O, H_2, CO and CO_2); R_i denotes the reaction rate of the gas component *i*; N_i represents the molar mass of the gas component *i*; r_j denotes overall rates of the reactions (*j*= 1, 2 and 3 corresponding to the Eq.s S8-10); The axial dispersion coefficient, $D_{ax,i}$ in the momentum balance equation was calculated by the Wakao correlation,[4] taking air at 400°C and 10^5 Pa as the reference; σ_{ij} is the stoichiometric coefficient of chemical component *i*, which is shown in Table S19.

The size parameters of the simulation, including the diameter of the catalyst and sorbent particles, the length of catalyst segment and absorbent segment, are consistent with the experimental results. The key parameters are shown in Table S20.

$$CH_4\,(g) + H_2O\,(g) \rightleftharpoons 3H_2\,(g) + CO\,(g), \quad \Delta H_r^{\Theta} = 205.9\ \text{kJ mol}^{-1} \tag{S5}$$

$$H_2O\,(g) + CO\,(g) \rightleftharpoons H_2(g) + CO_2\,(g), \quad \Delta H_r^{\Theta} = -41.1\ \text{kJ mol}^{-1} \tag{S6}$$

$$CH_4\,(g) + 2H_2O\,(g) \rightleftharpoons 4H_2(g) + CO_2\,(g), \quad \Delta H_r^{\Theta} = 164.8\ \text{kJ mol}^{-1} \tag{S7}$$

The flow field, temperature field and species distribution within the reactor are modeled and analyzed by the method. For simplicity of analysis, only the three reactions, Eq.s S5 to S7 are considered to take place in the reactor. Their reaction rates are expressed as follows according to Xu and Froment,[5] respectively:

$$r_1 = k_{as}\frac{k_1 P_{H_2}^{-2.5}\left(P_{CH_4}P_{H_2O} - P_{H_2}^3 P_{CO}K_{eq,1}^{-1}\right)}{DEN^2} \tag{S8}$$

$$r_2 = k_{as}\frac{k_2 P_{H_2}^{-1}\left(P_{CO}P_{H_2O} - P_{H_2}P_{CO_2}K_{eq,2}^{-1}\right)}{DEN^2} \tag{S9}$$

$$r_3 = k_{as}\frac{k_3 P_{H_2}^{-3.5}\left(P_{CH_4}P_{H_2O}^2 - P_{H_2}^4 P_{CO_2}K_{eq,3}^{-1}\right)}{DEN^2} \tag{S10}$$

$$DEN = 1 + K_{H_2}P_{H_2} + K_{CH_4}P_{CH_4} + K_{CO}P_{CO} + K_{H_2O}\frac{P_{H_2O}}{P_{H_2}} \tag{S11}$$

where k_j is reaction rate constant of reaction *j*; K_i is adsorption constant of chemical species *i*; $K_{eq,j}$ is thermodynamic equilibrium constant of reaction *j*; P_i is partial pressures of chemical species *i;* k_{as} is a fitting

parameter that reflects change in support/particle size/loading relative to the catalyst employed by Xu & Froment.[5] The values of those parameters are shown in Table S20.[6]

In this study, the hydrogen permeation membrane is made of Pd-Ag alloy, and the hydrogen flux is determined by the diffusion coefficient, the concentration gradient and the thickness of the membrane:[7]

$$J_{\mathrm{H_2}} = k_{\mathrm{bs}} \frac{k\left(P_{\mathrm{H_2,in}}^{n} - P_{\mathrm{H_2,out}}^{n} \right)}{d_{\mathrm{M}}} \tag{S12}$$

$$k = \mathrm{A} \exp^{-\frac{E_{\mathrm{A}}}{RT}} \tag{S13}$$

where n is an exponent, and it equals 0.62 which fits well in the experiment between 350°C and 900°C,[8] d_{M} is the thickness of membrane, k is the rate constant, A is the frequency or pre-exponential factor, which is 3.21×10^{-8}, and $\exp^{-\frac{E_A}{RT}}$ is the fraction of collisions that have enough energy to react (i.e., have energy greater than or equal to the activation energy E_{A} (equals 13410 J mol^{-1} in this work)) at temperature T. k_{bs} is a fitting parameter that reflects change in support/membrane relative to the membrane employed by Tong et. al.[9] In some other study, the applicable temperature range of Eq. S12 is extended down to 27°C.[10] For simplicity of analysis and discussion below, the temperature range was expanded from 300°C to 700°C reasonably.

An elementary reaction kinetics model related with Elovich type kinetic coefficient was adopted here to describe the CO_2 adsorption capacity and adsorption kinetic behavior of hydrotalcite. The mathematic equations of the adsorption model are:[11]

$$\frac{dq_{\mathrm{A}}}{dt} = k_{1\mathrm{f}} q_{\mathrm{O(s)}} \left(\frac{p_{CO_2}}{p_0} \right)^{c} - k_{1\mathrm{b}} q_{\mathrm{A}} - k_{2\mathrm{f}} q_{\mathrm{E}} q_{\mathrm{A}} + k_{2\mathrm{b}} q_{\mathrm{B}} - k_{3\mathrm{f}} q_{\mathrm{D}} q_{\mathrm{A}} + k_{3\mathrm{b}} q_{\mathrm{C}} \tag{S14}$$

$$\frac{dq_{\mathrm{B}}}{dt} = k_{2\mathrm{f}} q_{\mathrm{E}} q_{\mathrm{A}} - k_{2\mathrm{b}} q_{\mathrm{B}} \tag{S15}$$

$$\frac{dq_{\mathrm{C}}}{dt} = k_{3\mathrm{f}} q_{\mathrm{D}} q_{\mathrm{A}} - k_{3\mathrm{b}} q_{\mathrm{C}} \tag{S16}$$

$$x_{\mathrm{K}} = \frac{q_{\mathrm{B}} + q_{\mathrm{E}}}{q_{\mathrm{C}} + q_{\mathrm{D}}} \tag{S17}$$

$$q_{\mathrm{total}} = q_{\mathrm{B}} + q_{\mathrm{C}} + q_{\mathrm{D}} + q_{\mathrm{E}} \tag{S18}$$

where $q_{O(s)}$, q_A, q_B, q_C, q_D and q_E represent the corresponding site concentrations in elementary reaction model of hydrotalcite sorbent, which assumes that there are three types of CO_2 adsorption sites on the surface of hydrotalcite. The total site concentrations q_{total} of B, C, D, E and the ratio of K-related site to not-related site can be obtained if the sorbent is chosen.

The reaction rate k_i is calculated according to the Arrhenius form kinetic expressions:

$$k_i = A_i \exp\left(-\frac{E_i}{RT}\right) \tag{S19}$$

The activation energy E_{1f} and E_{1b} are described by:

$$E_{1f} = E_{1f}^0 + \alpha \frac{q_A}{q_{AS}} \tag{S20}$$

$$E_{1b} = E_{1b}^0 - \beta \frac{q_A}{q_{AS}} \tag{S21}$$

The fitted values of kinetic parameters are listed in Table S20. The flow in membrane reactor is assumed to be plug flow, and the major changes of hydrogen flux, cumulative CO_2 adsorption and methane conversion rates are distributed along the axial direction (Fig. S4). The cumulative CO_2 adsorption of hydrotalcite in one cycle is depicted in Fig. S15. The 85.0 mL (STP) of CO_2 adsorbed in hydrogen separation step is captured in CO_2 separation step. Besides, the SMR and water gas shift (WGS) processes are simultaneously achieved due to the decrease in reforming temperature by 400-600°C compared with conventional SMR approaches. Thus, the concentration ratio of CO remains in a low level through sequential separation of CO_2, which increases the lifetime of membrane. Moreover, nearly 100% conversion of methane at 400°C is implemented by sequential separation of products.

Model fitting

The elementary reaction kinetics model of hydrotalcite was comprehensively validated by experimental data from both ambient pressure thermogravimetric analysis (TGA) and a high-pressure adsorption apparatus in our previous study.[11] The elevated-temperature pressure swing adsorption (PSA) system modeling framework is then developed on the gPROMS® commercial simulation platform by

further considering comprehensive coupling effects of mass, momentum and energy transport processes, integrated with dynamic boundary condition and realistic operating procedures.[12] k_{as} and k_{bs} are the fitting parameters that reflect change in support/particle size/loading relative to the catalyst employed by Xu & Froment,[5] and change in support/membrane relative to the membrane employed by Tong et. al.[9] To validate the entire model with consideration of the kinetics of SMR reaction, hydrogen permeable membrane and hydrotalcite sorbent, the methane conversion rate and hydrogen production rate from the experiment were used for comparison (Fig. S16). Ten cycles of sequential separation-driven SMR experiment were performed and the results agree well with simulation results (relative error < 3%). As for the desorption process, the data of hydrotalcite at different temperatures and carbon dioxide partial pressures were used to calibrate the model. The SMR experiment was also performed with 3 alternating sets of catalyst and hydrotalcite for sequential separation, and experimental result (methane conversion rate 77.6%) was close to simulation result (methane conversion rate 76.2%), which further validated the simulation model's effectiveness under different material filling schemes.

Supplementary Text

Thermodynamic derivation of separation work

The principle of sequential separation of multiple products for chemical reaction as an effective means of enhancing conversion and equivalently lowering temperature is analyzed thermodynamically. For the global reaction combining methane steam reforming and water-gas shift (i.e., Eq. 3 of the main text) reactions:

$$CH_4\,(g) + 2H_2O\,(g) \rightleftharpoons 4H_2(g) + CO_2\,(g), \quad \Delta H_r^{\ominus} = 164.8\ \text{kJ mol}^{-1} \tag{S22}$$

and reaction conditions

$$n_{CH_4} = 1\ \text{mol}, n_{H_2O} = 2\ \text{mol}, T = 400°\text{C}, P_{tot} = 10^5\ \text{Pa}$$

the correlation between partial pressure of products and extent of reaction for single separation is expressed by:

$$\frac{\xi(3-2\xi)^2}{4(1-\xi)^3}=K_{\mathrm{P}}^{\Theta}(T)\frac{\left(P^{\Theta}\right)^2\left(P^{\Theta}-P_1\right)^2}{\left(P_1\right)^4} \tag{S23}$$

where ξ is extent of reaction, which describes the degree of chemical reaction progress; P^{Θ} is standard pressure, which is usually taken as 10^5 Pa; P_1 is the separation pressure of hydrogen; $K_{\mathrm{P}}^{\Theta}(T)$ is thermodynamic equilibrium constant for the overall reaction of SMR and WGS; T is reaction temperature. The correlation between ideal separation work consumption and extent of reaction for single-product separation is calculated by Eq. S24:

$$W_{\mathrm{sep1}}=W_{\mathrm{sep,H_2}}=4\xi RT_0\ln\left(\frac{P_0}{P_1}\right) \tag{S24}$$

where W_{sep1} and $W_{\mathrm{sep,H_2}}$ are the separation work consumption of single separation and hydrogen separation, respectively; R is the universal gas constant, which is 8.314 J mol^{-1} K^{-1}; T_0 is ambient temperature, which is 298.15 K. The correlation between partial pressure of products and extent of reaction for sequential separation of H_2 and CO_2 is calculated by:

$$n_k=\frac{4\xi_{\mathrm{e}}}{1-\xi_{\mathrm{e}}}\left(1-\xi_{\mathrm{e}}-\sum_{i=1}^{2\mathrm{k}}\Delta\xi_i\right) \tag{S25}$$

$$K_{\mathrm{P}}^{\Theta}(T)=\frac{(n_k-4\Delta\xi_{2k})^2\left[\frac{P^{\Theta}-P_2}{P_2}(n_k-4\Delta\xi_{2k})-3\left(1-\xi_{\mathrm{e}}-\sum_{i=1}^{2k\text{-}1}\Delta\xi_i\right)\right]}{4\left(\frac{P^{\Theta}}{P_2}\right)^2\left(1-\xi_{\mathrm{e}}-\sum_{i=1}^{2k\text{-}1}\Delta\xi_i\right)^3} \tag{S26}$$

$$K_{\mathrm{P}}^{\Theta}(T)=\frac{\mathrm{n}_k^5}{16\left(1-\xi_{\mathrm{e}}-\sum_{i=1}^{2k}\Delta\xi_i\right)^3\left[3\left(1-\xi_{\mathrm{e}}-\sum_{i=1}^{2k}\Delta\xi_i\right)+1.25n_k\right]^2} \tag{S27}$$

where k is the total number of sets of catalyst-sorbent combination; n_k is the molar amount of hydrogen after k$^{\mathrm{th}}$ alternating separation of hydrogen and carbon dioxide to the chemical equilibrium state, respectively; P_2 is the separation pressure of hydrogen. The $\Delta\xi_i$ is calculated by the function relation of

$\Delta\xi_i = f\left(K_{\mathrm{P}}^{\Theta}(T), P_2, P^{\Theta}\right)$. The correlation between ideal separation work and extent of reaction for sequential separation of H_2 and CO_2 is calculated by Eq. S28:

$$W_{\mathrm{sep2}} = W_{\mathrm{sep,H_2}} + W_{\mathrm{sep,CO_2}} = \sum_{i=2m\text{-}1}^{2k-1} \Delta\xi_i RT_0 \ln\left(\frac{P_0}{P_2}\right) + \sum_{i=2m}^{2k} \Delta\xi_i RT_0 \ln\left(\frac{P_0}{P_3}\right) \quad \left(m \in \mathbb{N}^+,\ m \le k\right) \tag{S28}$$

where W_{sep2} and $W_{\mathrm{sep,CO_2}}$ are the ideal work consumption of sequential separation and carbon dioxide separation, respectively. P_3 is the separation pressure of CO_2. The work of separation derived by Eq. S28 only considers species that are physically separated from the system, i.e., H_2 and CO_2, that incur separation work.

Indirectly heated solar sequential separation-driven SMR

In indirectly heated solar sequential separation-driven SMR, concentrated solar thermal energy (350-400°C) via parabolic trough collector heats up the heat transfer fluid, which then provides the mid-temperature heat for methane reforming (Fig. 4E). Such indirect solar reformer design is advantageous for stable hydrogen production by eliminating fluctuations in solar illumination via thermal energy storage. In contrast, directly illuminated solar methane reformers also serve as solar thermal energy receiver simultaneously, and radiative loss to the ambient could often become the dominant form of energy loss due to the relatively slow kinetics of the reforming reaction. The indirectly heated reformer decouples solar heat collection and methane reforming reaction temporally, which opens up possibilities for efficiency and continuous solar H_2 production.

Efficiency Calculation

(1) Maximum thermochemical efficiency of sequential separation-driven SMR (Table S21).

$$\eta = \frac{n_{\mathrm{H_2}} \cdot \Delta H_{\mathrm{H_2}} + n_{\mathrm{CO}} \cdot \Delta H_{\mathrm{CO}} - n_{\mathrm{CH_4}} \cdot \Delta H_{\mathrm{CH_4}}}{Q_{\mathrm{input}} + W_{\mathrm{penalty}} \cdot \eta_{\mathrm{th\text{-}ele}}^{-1}} \tag{S29}$$

where $n_{\mathrm{H_2}}$ and n_{CO} are the molar amounts of H_2 and CO produced, respectively, and $n_{\mathrm{CH_4}}$ is the net amount of methane consumed; $\Delta H_{\mathrm{H_2}}$, ΔH_{CO} and $\Delta H_{\mathrm{CH_4}}$ are the higher heating values of H_2, CO and

CH_4, respectively, Q_{input} is the thermal energy input required to drive the conversion of n_{CH_4} mole of methane to H_2 and CO_2. If we take n_{CH_4} as 1 mol, Q_{input} includes reaction enthalpy change (164.8 kJ mol^{-1}) and reactant preheating energy (131.6 kJ mol^{-1}). W_{penalty} is separation work (27.2 kJ mol^{-1}) for both H_2 and CO_2, and $\eta_{\text{th-ele}}$ is thermal-to-electric conversion efficiency, which is taken as the Carnot efficiency at the corresponding reaction temperature. Thus for the sequential separation-driven SMR at 400°C, the maximum thermochemical efficiency is 73.2%.

(2) Solar-to-hydrogen efficiency in directly heated solar sequential separation-driven SMR

In this work, CH_4 reforming is driven by directly concentrated solar energy (heat). Solar-to-hydrogen efficiency is defined as follows:

$$\eta_{\text{solar-H}_2}=\frac{n_{CH_4}\left(4\Delta H_{H_2}-\Delta H_{CH_4}\right)}{Q_{\text{input}}+W_{\text{penalty}}\cdot\eta_{\text{th-ele}}^{-1}}=\frac{n_{CH_4}\left(4\Delta H_{H_2}-\Delta H_{CH_4}\right)}{Q_{\text{input}}+\left(\frac{W_{\text{pump,H}_2}}{\eta_{\text{pump}}}+\frac{W_{\text{inert}}}{\eta_{\text{regen}}}\right)\cdot\eta_{\text{sol-ele}}^{-1}} \tag{S30}$$

where Q_{input} is the total solar thermal energy input, and is provided by concentrated solar energy, with the measured average solar direct normal irradiance (DNI) being 160 W m^{-2}. Under such illumination conditions, Q_{input} is 6580.2 kJ mol^{-1} for driving 1 mole of methane reforming into H_2 and CO_2 (conversion rate of 95%); CO_2 is separated by inert gas sweeping, and the inert gas could be regenerated by a CO_2-permeable selective membrane. W_{inert} is the theoretical separation work of the mixed gas. η_{regen} is compressor efficiency (taken as 85%).[13] H_2 separation is driven by a vacuum pump, the efficiency η_{pump} of which is given by:[14]

$$\eta_{\text{pump}}=0.07\cdot\log\left(\frac{p_{\text{total}}}{p_{\text{atmospheric}}}\right)+0.4 \tag{S31}$$

In the experiment, hydrogen is pumped out at 5000 Pa, and the efficiency of the vacuum pump η_{pump} at the corresponding pressure is 30.9%. Note that $\eta_{\text{solar-H}_2}$ is weakly dependent on η_{pump} because $Q_{\text{input}} >> W_{\text{pump, H}_2}$ in directly heated solar sequential separation-driven SMR. A solar PV module with

the conversion efficiency $\eta_{\text{sol-ele}}$ of 30% is assumed to provide the separation work, and the solar energy required for product separation is 336.6 kJ mol^{-1}. For the directly heated solar sequential separation-driven SMR at 400°C, the solar-to-hydrogen efficiency is 3.4%.

(3) Solar-to-hydrogen efficiency in indirectly heated solar sequential separation-driven SMR

In this study, the solar reforming reactor was operated with commercially available Ni catalyst, hydrotalcite (HTC) CO_2 adsorbent, vacuum pump, inert gas, and was integrated with direct solar illumination. Such non-optimized conditions imposed both thermodynamic and kinetic limitations on the thermochemical efficiency, resulting in the low value of 3.4% as reported.

As for the directly heated solar sequential separation-driven SMR, the Q_{th} term consists primarily of the total amount of solar energy incident onto the reactor, which is directly proportional to the accumulated time of illumination (assuming constant irradiation intensity of sunlight). However, only a very small portion of this energy is taken by the endothermic global SMR reaction, primarily due to the slow kinetics of the Ni catalyst for the SMR reaction and HTC sorbent for adsorbing and desorbing CO_2. The heat transfer process for providing reaction heat also incurs considerable energy loss to the ambient. As shown in Table S21, the experimentally measured solar energy input equals 6580.2 kJ for each mole of CH_4 converted, while the thermal energy intake of the global SMR reaction is only 156.5 kJ. It means that most of the energy supply is dissipated (as re-radiation loss from the solar receiver tube / reactor) to the ambient, instead of being timely converted to the chemical energy of the fuel.

If solar energy could be collected by heat transfer fluid, such as thermal oil or molten salt, then not only the solar thermal energy could be stored for a much longer period and the reactor could be well insulated, but the solar heat could also be supplied to the reactor from both inside and outside, dramatically reducing heat transfer energy losses. Most importantly, storage of the solar thermal energy would allow for relatively slow kinetics of the (non-optimized) catalyst and sorbent, so that a significantly lower amount of solar thermal energy is needed for producing the same amount of fuel. Alternatively, if the kinetics of SMR catalyst and CO_2 sorbent could be “fast enough”, then the reactor could be operated with high efficiency with direct solar illumination, and the storage of solar thermal energy may become unnecessary. The solar-to-hydrogen efficiency (Eq. S30) can be further expanded as:

$$\eta_{\text{solar-H}_2} = \frac{n_{\text{CH}_4}\left(4\Delta H_{\text{H}_2} - \Delta H_{\text{CH}_4}\right)}{Q_{\text{input}} + W_{\text{penalty}} \cdot \eta_{\text{th-ele}}^{-1}} = \frac{n_{\text{CH}_4}\left(4\Delta H_{\text{H}_2} - \Delta H_{\text{CH}_4}\right)}{\frac{Q_{\text{reaction}}}{\eta_{\text{ex}} \cdot \eta_{\text{abs}}} + \frac{Q_{\text{preheating}}}{\eta_{\text{ex}} \cdot \eta_{\text{abs}}} \cdot (1 - \eta_{\text{rec}}) + \left(\frac{W_{\text{pump,H}_2}}{\eta_{\text{pump}}} + \frac{W_{\text{inert}}}{\eta_{\text{regen}}}\right) \cdot \eta_{\text{sol-ele}}^{-1}} \quad \text{(S32)}$$

For indirectly heated solar sequential separation-driven SMR, the reactor is heated by solar heat transfer fluid. Solar-to-heat efficiency η_{abs} of 95% (calculated from Chen et al.),[15] heat exchange efficiency η_{ex} of 88%,[16] and heat recovery efficiency η_{rec} of 90% are assumed.[17] Q_{reaction} is the enthalpy change of the global SMR reaction, and $Q_{\text{preheating}}$ is the enthalpy change for reactants preheating from 25℃ to 400℃. $W_{\text{pump,H}_2}$ is the pumping work for hydrogen separation, for which H_2 is assumed to be separated by an electrochemical hydrogen pump, and the separation work is 19.7 kJ mol^{-1}-H_2. Electrochemical hydrogen pump efficiency (85%) is calculated based on the literature [18] with consideration of the irreversible losses (i.e., activation polarization, ohimc and sheet overpotentials) in actual electrochemical separation process. CO_2 is separated by inert gas sweeping, and the inert gas could be regenerated by a selective CO_2-permeable membrane. W_{inert} is the theoretical work consumption for the regeneration of the inert gas from the gas mixture (inert gas and CO_2). η_{regen} is compressor efficiency, taken as 85%,[13] and the actual work consumption for the regeneration of the inert gas ($W_{\text{inert}}/\eta_{\text{regen}}$) is 11.8 kJ mol^{-1}. Separation work is assumed to be provided by a solar PV cell with a conversion efficiency $\eta_{\text{sol-ele}}$ of 30%, so that the solar energy required for product separation is 302.2 kJ mol^{-1}. Thus for the sequential separation-driven SMR reaction at 400°C, the solar-to-hydrogen efficiency of the indirectly heated solar sequential separation-driven SMR is 46.5%.

ECSA® method

Mass spectrometer combined with equivalent characteristic spectrum analysis (ECSA®) is applied to analyze the dynamic changes in reaction. The gas species in the reaction process include Ar, CH_4, CO_2, CO, H_2, He and H_2O. Considering that N_2 and O_2 are the main components of air, the two gases are also taken into consideration. Each mass spectrometer equipment has its own working characteristics, i.e., characteristic spectrum and relative sensitivity. The mass spectrometer used in this work is calibrated

particularly by the nine gases above. All the experimental data are analyzed by the calibration results of characteristic spectrum and relative sensitivity.

A quadrupole mass spectrometer (Pfeiffer Omnistar GSD 320) is employed for experiment measurements. The working ionization energy is 70 eV, and the testing mass-to-charge ratio ranges from 2 to 50 amu. Sampling capillary works at 150°C.

The calibration of gases includes two parts: the calibration of characteristic spectrum and the calibration of relative sensitivity. The method of the calibration of characteristic spectrum of gas is similar to the calibration of the carrier gas. As for relative sensitivity, the gas to be calibrated is mixed with the carrier gas Ar. The detailed calibration process is explained in our previous work.[19]

Here the characteristic spectrum of all calibrated gases is summarized in Fig. S17. All data of the characteristic spectrum and relative sensitivity for nine gases are shown in Table S22.

Calculation of energy consumption of upgraded sequential separation-driven SMR processes

1) Assumptions:

a) The energy consumption calculation is based on the global SMR reaction at 400ºC

$$CH_4\ (g) + 2H_2O\ (g) \rightleftharpoons 4H_2(g) + CO_2\ (g),\ \Delta H_{400^oC} = 180.9\ kJ\ mol^{-1}$$

b) Conversion rate of CH_4, yield and selectivity of H_2 and CO_2 are all assumed to be 100%, based on experimental data of > 99% conversion rate of CH_4, and > 99% yield and selectivity of H_2 and CO_2 reported in our study.

c) In consistency with operating conditions of industrial SMR

i. Steam-to-methane ratio is chosen as 3.4.[20]

ii. Energy input required for heating steam at 200ºF (93ºC) and above is completely covered by heat recuperation via internal heat exchangers in consistency with industrial SMR process.[21]

iii. Energy input required by the endothermic global SMR reaction and for heating water from ambient temperature to 200ºF (93ºC) [21] is provided by burning methane for external heating, taking heat exchanger efficiency of 0.85 [22] into account.

iv. Energy consumption for CO_2 recovery is inherently included for H_2 production stage for both industrial SMR [20] and our method, but both excluding external heating.

d) Our method delivers H_2 with the same pressure as that of industrial SMR. In our method, separation

of both H_2 and CO_2 is driven by the partial pressure difference of each species, respectively. Therefore, our method shall also be able to work under pressurized conditions in industrial SMR for SMR reactor and pressure-swing adsorption (PSA) unit. For pressurized SMR reactor with H_2 permeation membrane, the H_2 permeation flux is proportional to the difference between the square root of the H_2 partial pressure on the reactor side and the square root of that on the permeate side across the membrane,[7, 23] and the integrated CO_2 adsorption / desorption process in our method shall work in the same way as the PSA process in industrial SMR.

2) Calculation:

a) For the complete conversion of 1 mole of CH_4 to H_2 and CO_2 by the global SMR reaction (Eq. S22), the total amount of CH_4 required as reactant and as fuel for heating purpose is:

i. Reaction heat required is 180.9 kJ, and energy required for heating 3.4 moles of H_2O from 25ºC to 93ºC is 17.4 kJ. Therefore, the total thermal energy input required is (180.9+17.4)/0.85 = 233.3 kJ.

ii. The thermal energy input is converted to the amount of methane required by the lower heating value of methane (800.2 kJ mol^{-1}), i.e., 233.3/800.2 = 0.292 mol.

iii. In the global SMR reaction, each mole of CH_4 produces 4 moles of H_2 (8 grams).

iv. Thus, each kg of H_2 requires a total input of CH_4: (1+0.292) ×1000/8×890.6 = 143.6 MJ.

b) Electricity consumption for delivering pressurized H_2 and separating CO_2. We take 450 psia (30.6 bar) reactor pressure and 346 psia (23.5 bar) H_2 outlet pressure [20] as the condition for operating the sequential separation-driven SMR reactor.

i. Ideal electricity consumption for delivering the pressurized H_2 is $R \cdot T \cdot \ln(P_{reactor}/P_{H2,out})$ = 8.314×(400+273.15)×ln (450/346) = 1.47 kJ mol^{-1}-H_2. Furthermore, we take the efficiency of mechanical compressor as 0.85 for the pressurization of reactor.[7] Therefore, the actual electricity consumption for delivering 1 kg of pressurized H_2 is 1.47×1000/2/0.85 = 0.86 MJ.

ii. Electricity consumption for separating CO_2 can be considered as the same as that of pressurizing the reactor and PSA separation in industrial SMR. In the industrial PSA unit, the pressure varies between 24 bar and 0.3 bar, and CO_2 is the major species being separated.[24] The entire process of separation of CO_2 requires pressurizing / depressurizing the reactor (in our study; or equivalently the PSA unit in industrial SMR) and driving the flow through the

entire process. Therefore, the electricity consumption for separating CO_2 can be considered the same as that for industrial SMR, i.e., 2.04 MJ mol^{-1}-H_2.[20]

Therefore, the total electricity consumption of the sequential separation-driven SMR amounts to 0.86 + 2.04 = 2.90 MJ mol^{-1}-H_2.

Calculation of energy consumption of industrial SMR process (for comparison)

In this part, most of the data are directly from Ref. [20]. For the production of 1.5 million Nm^3-H_2 day^{-1}, the direct accounting for methane input as reactant feed and for heating are 392 Mg day^{-1} (million grams per day) and 43 Mg day^{-1}, respectively. However, the conversion of methane industrial SMR is 80%, which means that the unconverted methane is then burnt for heating purposes as well. Therefore, the real amounts of methane for reactant feed and for heating are 313.6 Mg day^{-1} and 121.4 Mg day^{-1}, respectively. As 1 Nm^3 amounts to 44.64 moles of ideal gas (89.3 g in the case of H_2), the two numbers of methane input are converted to 2.34 kg-CH_4 kg^{-1}-H_2 and 0.91 kg-CH_4 kg^{-1}-H_2, respectively. They sum to 3.25 kg-CH_4 kg^{-1}-H_2, equivalent to 180.9 MJ kg^{-1}-H_2. The electricity consumption for industrial SMR (for pressurizing the reactor, driving flow and driving the PSA unit) is 2.04 MJ kg^{-1}-H_2.

Techno-economic analysis

The levelized cost of hydrogen (LCOH) is calculated for both sequential separation-driven SMR system and industrial SMR system, considering all components of the cost breakdown. The LCOH is given by [25]

$$\mathrm{LCOH}=\frac{\sum_{t=1}^{n}\left[\left(I_t+M_t+F_t\right)\left(1+r\right)^{-t}\right]}{\sum_{t=1}^{n}\left(E_t\left(1+r\right)^{-t}\right)} \tag{S33}$$

where I_t is the investment (i.e., direct and indirect capital) expenditures in year t; M_t is the operation and maintenance (i.e., O&M) expenditures in year t; F_t is the fuel (i.e., feedstock) expenditures in year t; E_t is the amount of hydrogen produced in year t; r is the discount rate, taken as 15%; n is the expected lifetime of the system in years. In the LCOH formulation, all the I_t, M_t and F_t terms of the two systems are given in Tables S11 and S12, E_t is the annual H_2 production based on the 30 ton-H_2/day capacity, and n is the lifetime of the system (20 years).

The LCOH and its breakdown are summarized in Table S6 (details are further given in Tables S9 through S11). The LCOH of our method is projected to be 1.13 \$ kg^{-1}-H_2, which is 9% lower than that of industrial SMR with CO_2 capture.[20] This is primarily due to lower capital cost and feedstock cost, which are in turn due to significantly reduced reactor size, and higher conversion rate of methane, respectively, as compared with industrial SMR.

Supplementary Figures

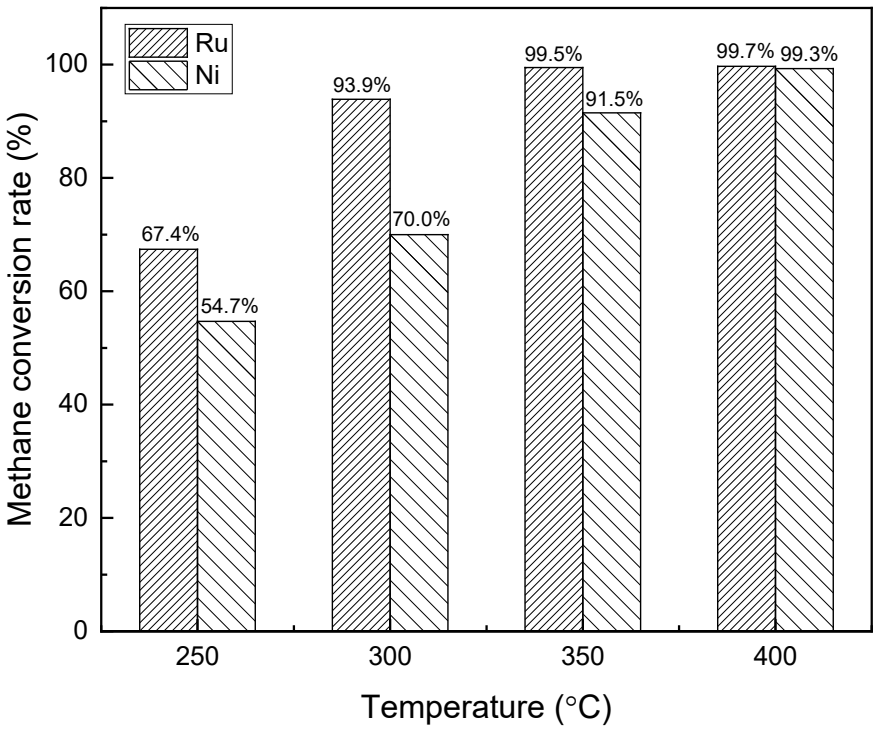

Fig. S1. Comparison of methane conversion rate for different catalysts of Ru and Ni for sequential separation-driven SMR reaction in the range of 250°C to 400°C.

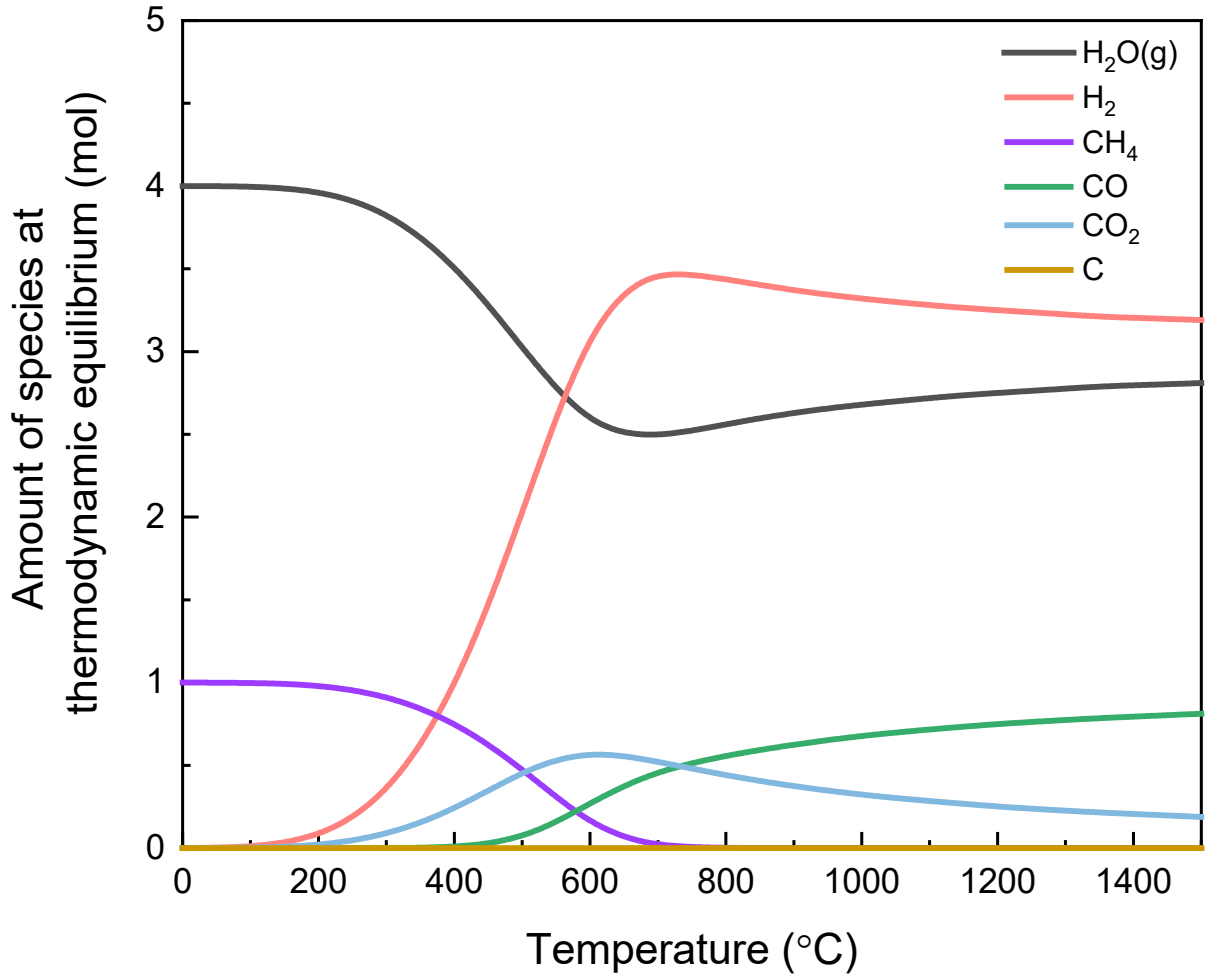

Fig. S2. Thermodynamic calculation of the amount of products of steam methane reforming in the temperature range of 0-1500°C.[26] For 1 mole of CH_4 and 4 moles of H_2O as reactants, solid carbon is less than 1×10^{-36} mole within the entire temperature range.

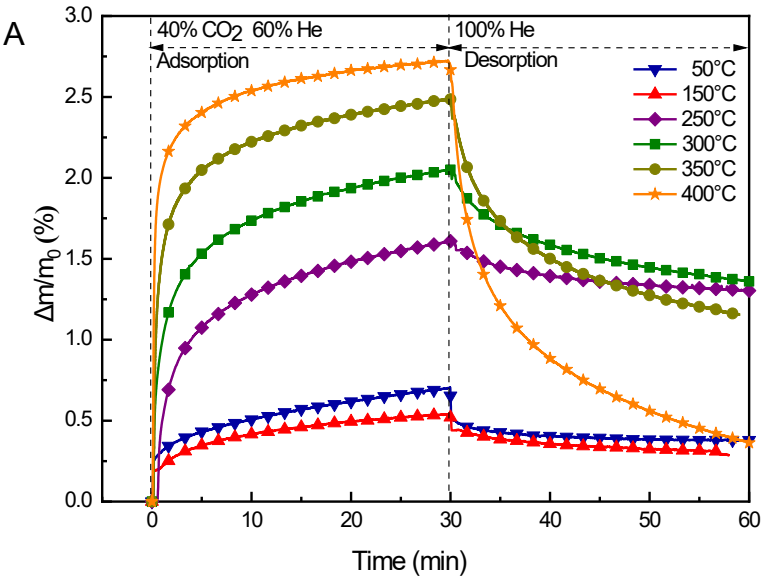
A
40% CO2 60% He
Adsorption
100% He
Desorption
50°C
150°C
250°C
300°C
350°C
400°C
Δm/m0 (%)
Time (min)

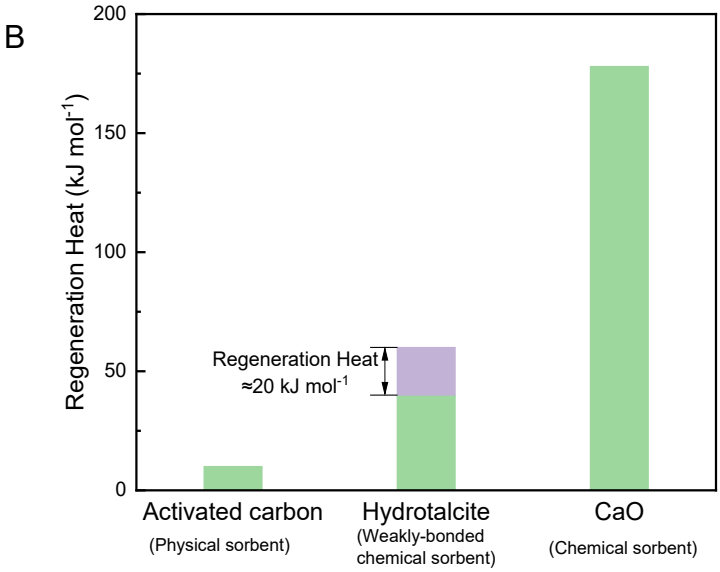
B
Regeneration Heat (kJ mol-1)
Regeneration Heat
≈20 kJ mol-1
Activated carbon
(Physical sorbent)
Hydrotalcite
(Weakly-bonded
chemical sorbent)
CaO
(Chemical sorbent)

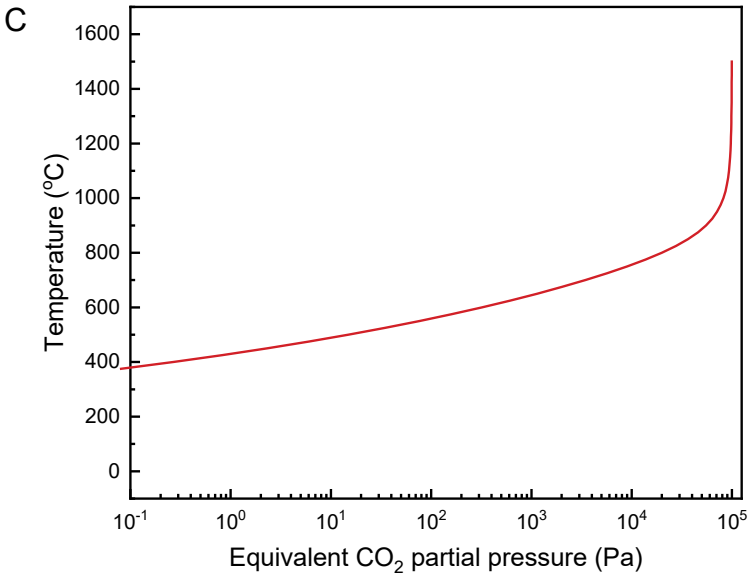
C
Temperature (°C)
Equivalent CO2 partial pressure (Pa)

Fig. S3. Adsorption-desorption performance of the hydrotalcite sorbent employed in this study, and the comparison of regeneration energy penalty with two other CO_2 sorbents. (A) Adsorption-desorption cycle of hydrotalcite; (B) Theoretical regeneration heat of activated carbon, hydrotalcite and CaO; (C) The relationship between equivalent CO_2 partial pressure and temperature for the regeneration of CaO (via $CaCO_3$ decomposition).[26]

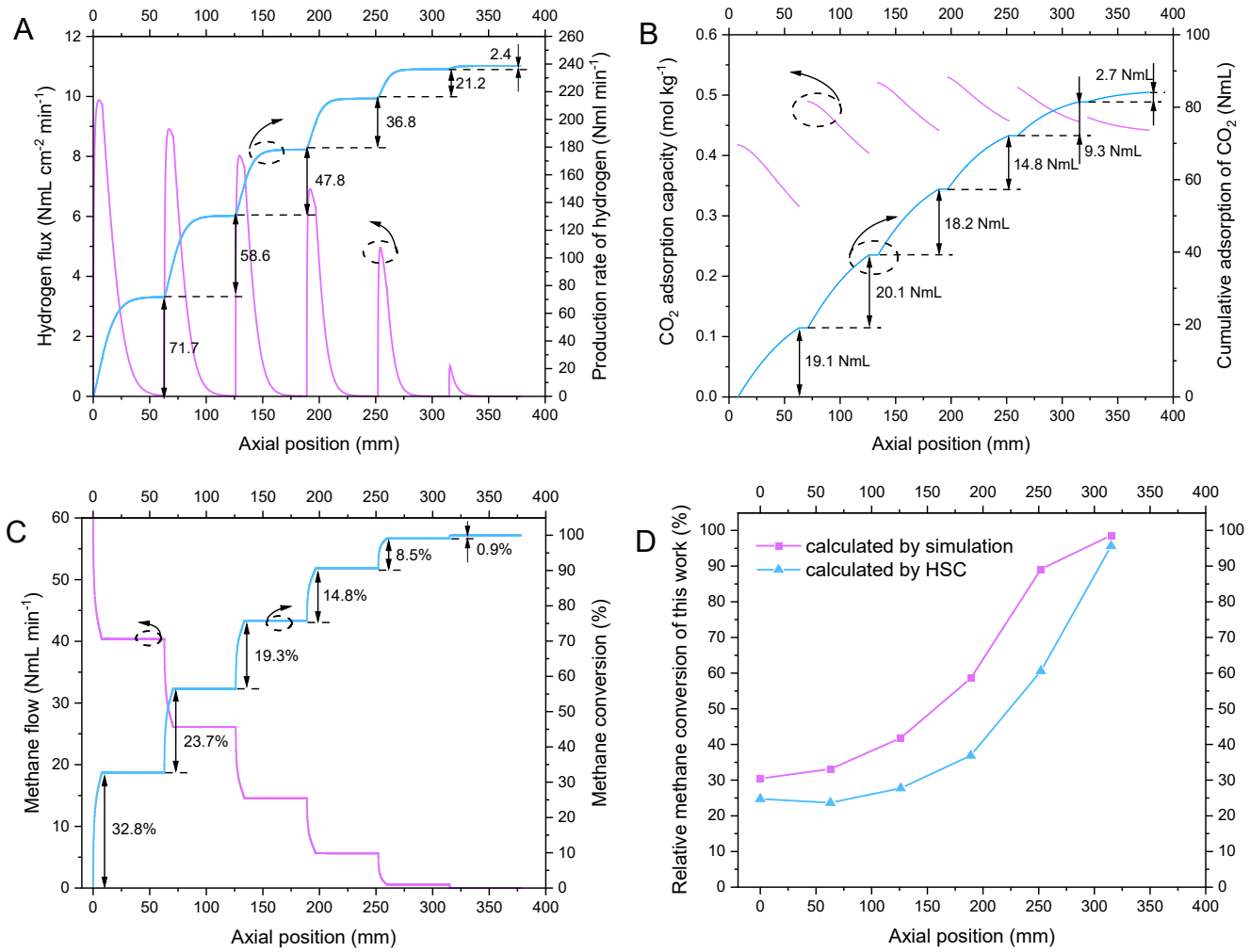

Fig. S4. Simulation results of the hydrogen separation step of the sequential separation-driven SMR cycle. (A) Hydrogen flux along the Pd-Ag membrane. (B) Cumulative CO_2 adsorption of hydrotalcite along axial position. (C) Methane flow along the axial direction. (D) Relative conversion of methane in each catalyst-sorbent set by simulation or thermodynamic calculation (by HSC software).[26] The hydrogen separation pressure of vacuum pump is 2000 Pa. The reaction temperature and pressure are 400°C and 10^5 Pa respectively. The inlet methane flow rate is 60 mL min^{-1} (STP) and the steam-to-methane ratio is 4. In one cycle, the periods of H_2 and CO_2 separation are 1.5 min and 9.0 min, respectively.

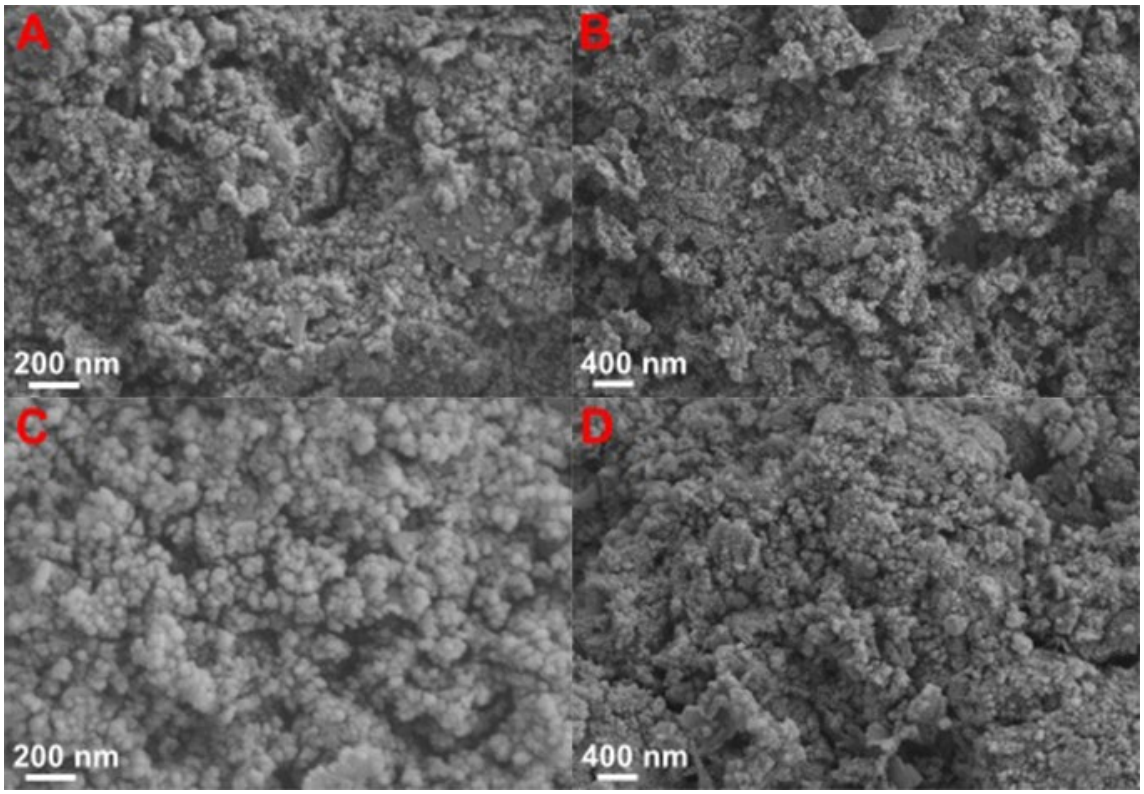

Fig. S5. Scanning electron microscopy images of the Ni (40 wt%) / MgO-Al_2O_3 catalyst. (A)(B) before reaction. (C)(D) after 6000 cycles.

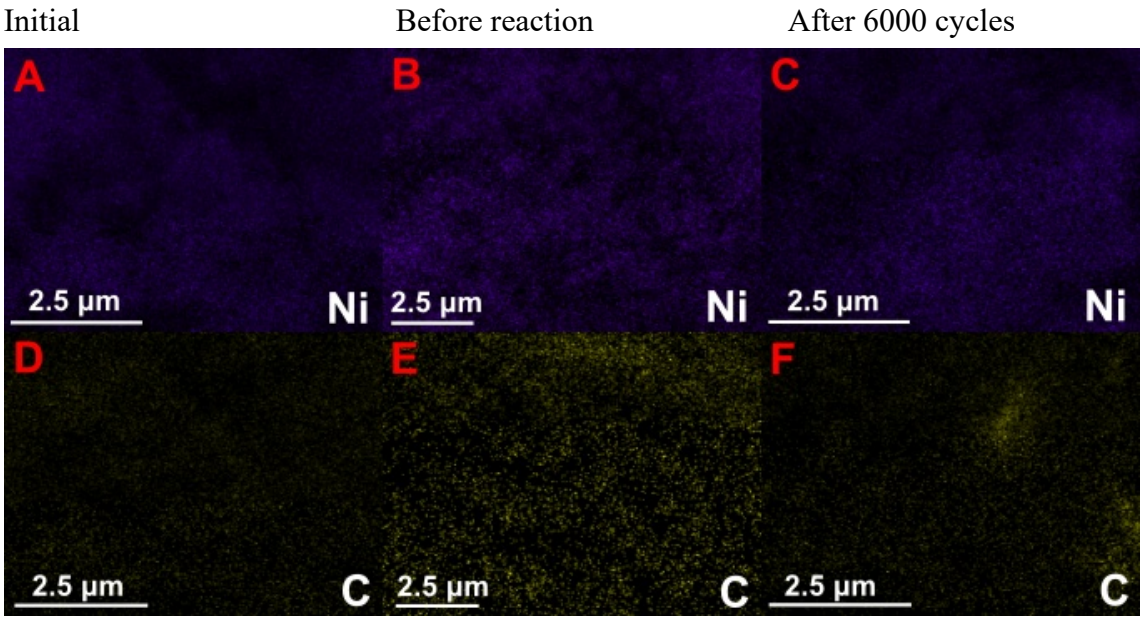

Fig. S6. Energy dispersive X-ray (EDX) spectroscopy elemental maps of the Ni (40 wt%) / MgO-Al_2O_3 catalyst for initial, before-reaction and post-6000-cycle states. (A)-(C) EDX elemental maps of Ni. (D)-(F) EDX elemental maps of C (The weight percentage of each element in the catalyst in the three states is shown in Table S23).

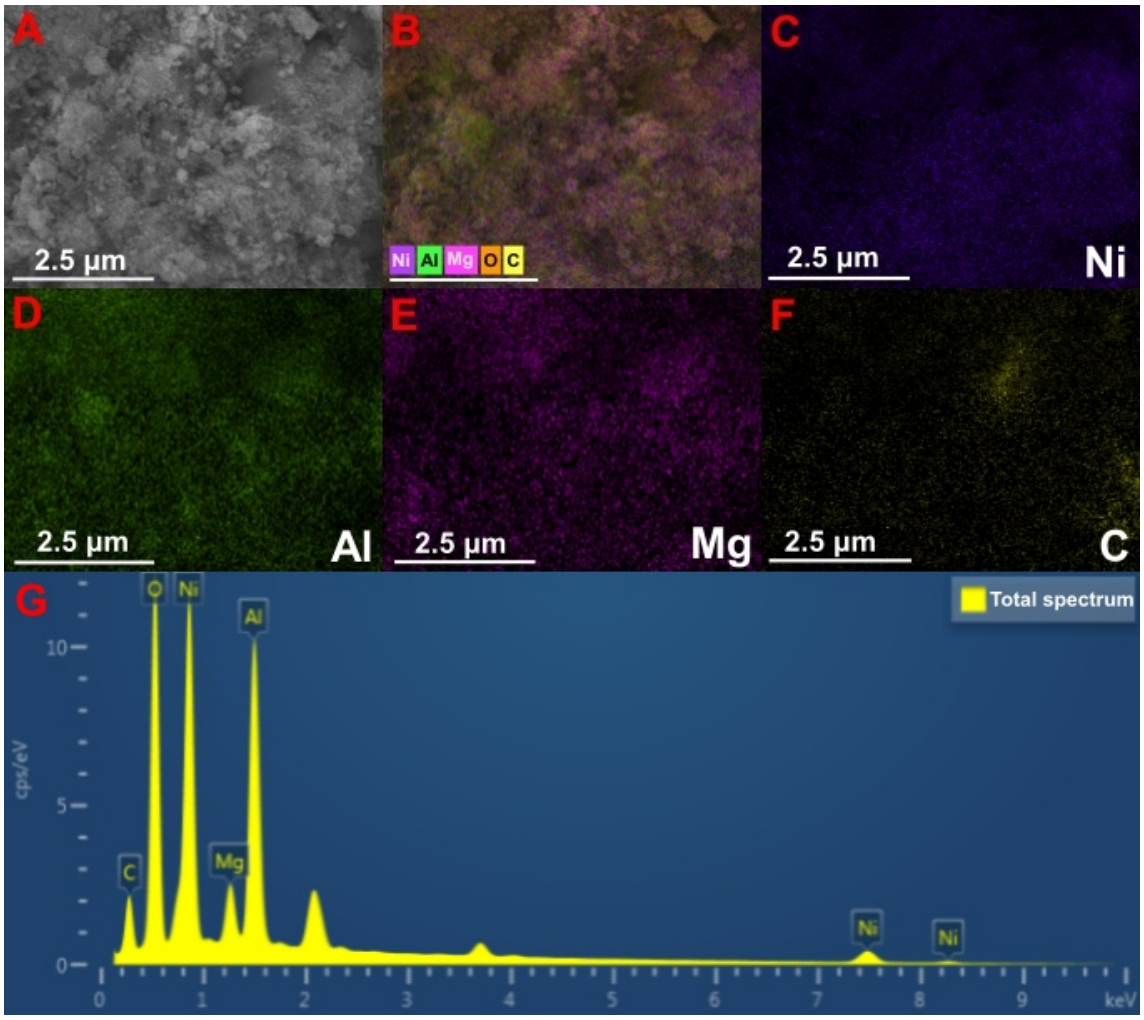

Fig. S7. Scanning electron microscopy (SEM) images and Energy dispersive X-ray (EDX) spectroscopy images of the Ni (40 wt%) / MgO-Al_2O_3 catalyst after 6000 cycles. (A) SEM image. (B)-(F) EDX elemental maps of the Ni (40 wt%) / MgO-Al_2O_3 catalyst. (G) EDX mapping.

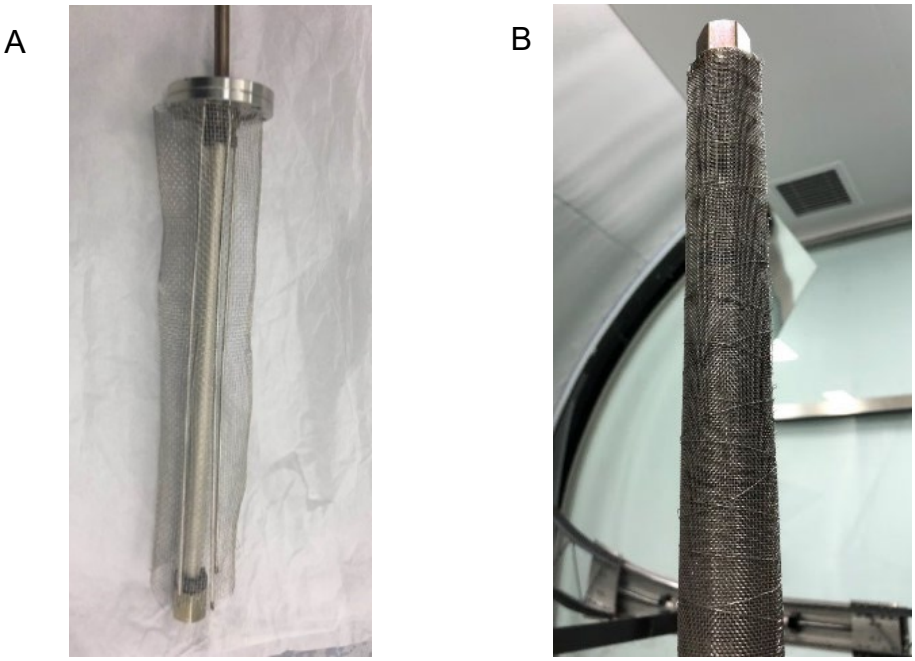

Fig. S8. Sequential separation-driven SMR reactor for integration with parabolic trough solar collector. (A) The Pd-Ag membrane tube wrapped by a stainless-steel mesh. (B) The Pd-Ag membrane tube with a stainless-steel mesh housing six sets of Ni/MgO-Al_2O_3 catalyst and hydrotalcite CO_2 sorbent combination.

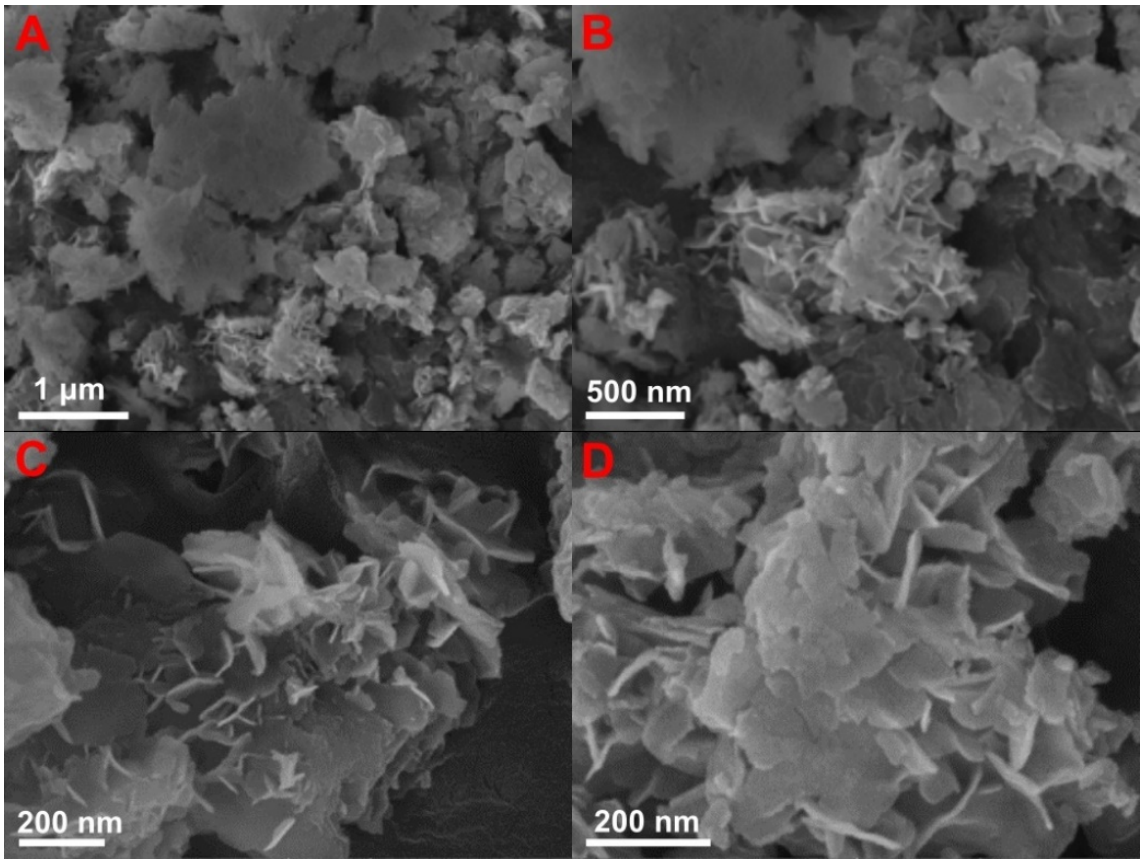

Fig. S9. Scanning electron microscopy images of the K-promoted (20 wt%) MgAl-layered double oxide composite at different scales.

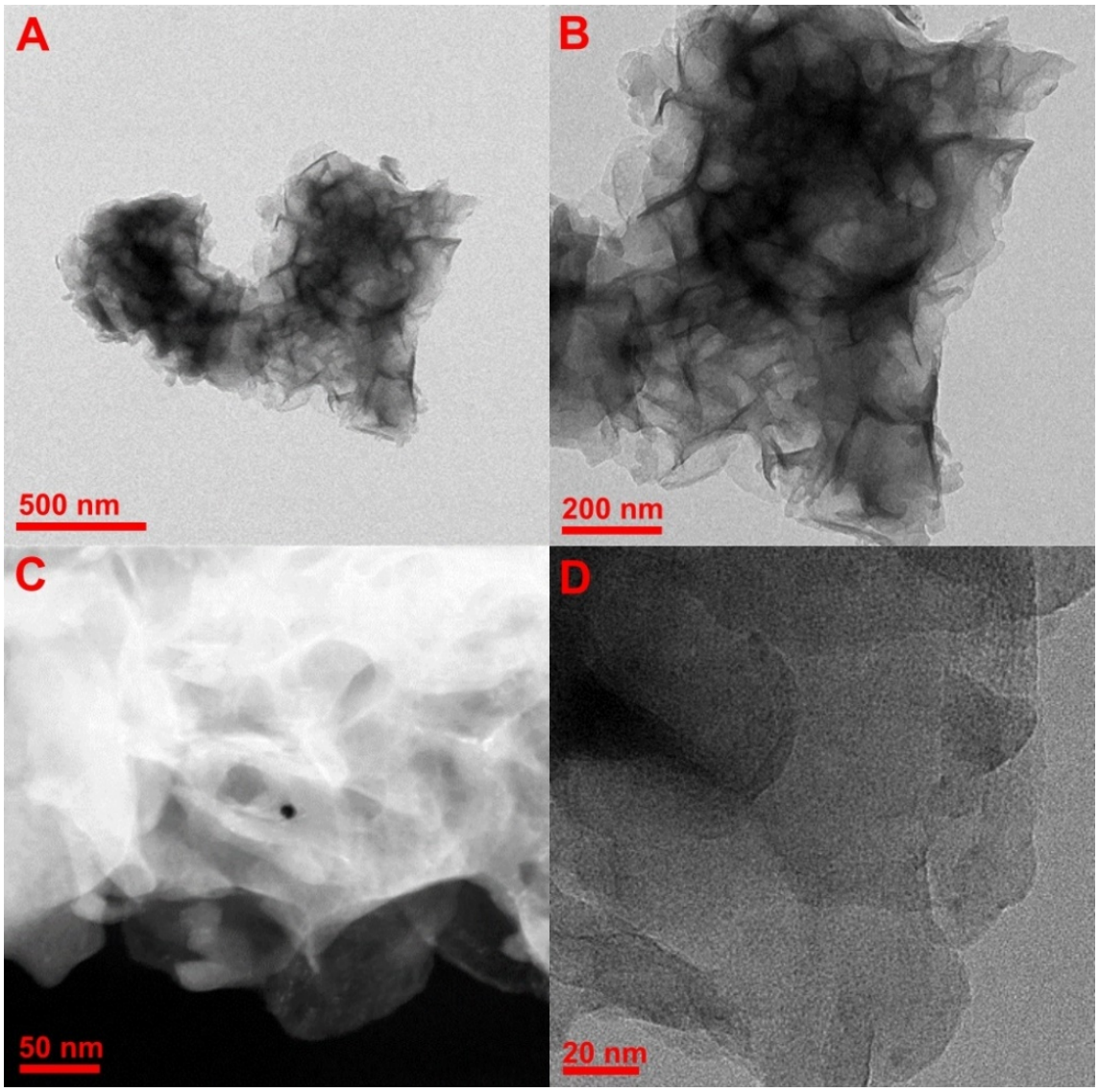

Fig. S10. Transmission electron microscopy images of the K-promoted (20 wt%) MgAl-layered double oxide composite at different scales.

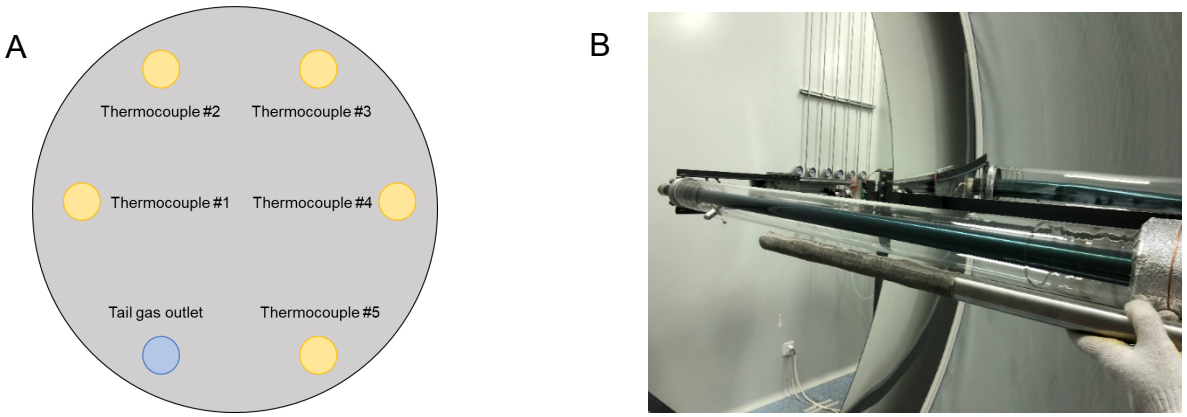

Fig. S11. Measurement of temperature distribution within the sequential separation-driven SMR reactor integrated with parabolic trough solar collector receiver tube. (A) Deployment of thermocouples on the cross-section of the reactor; (B) Depth of the reactor into the receiver tube.

Fig. S12. Experimental platform for proof-of-concept studies of sequential separation-driven SMR. (A) The reactor corresponding to Fig. 1 of the main text. (B) The reactor mounted in an electric furnace for measurements. (C) Online measurement and analysis system.

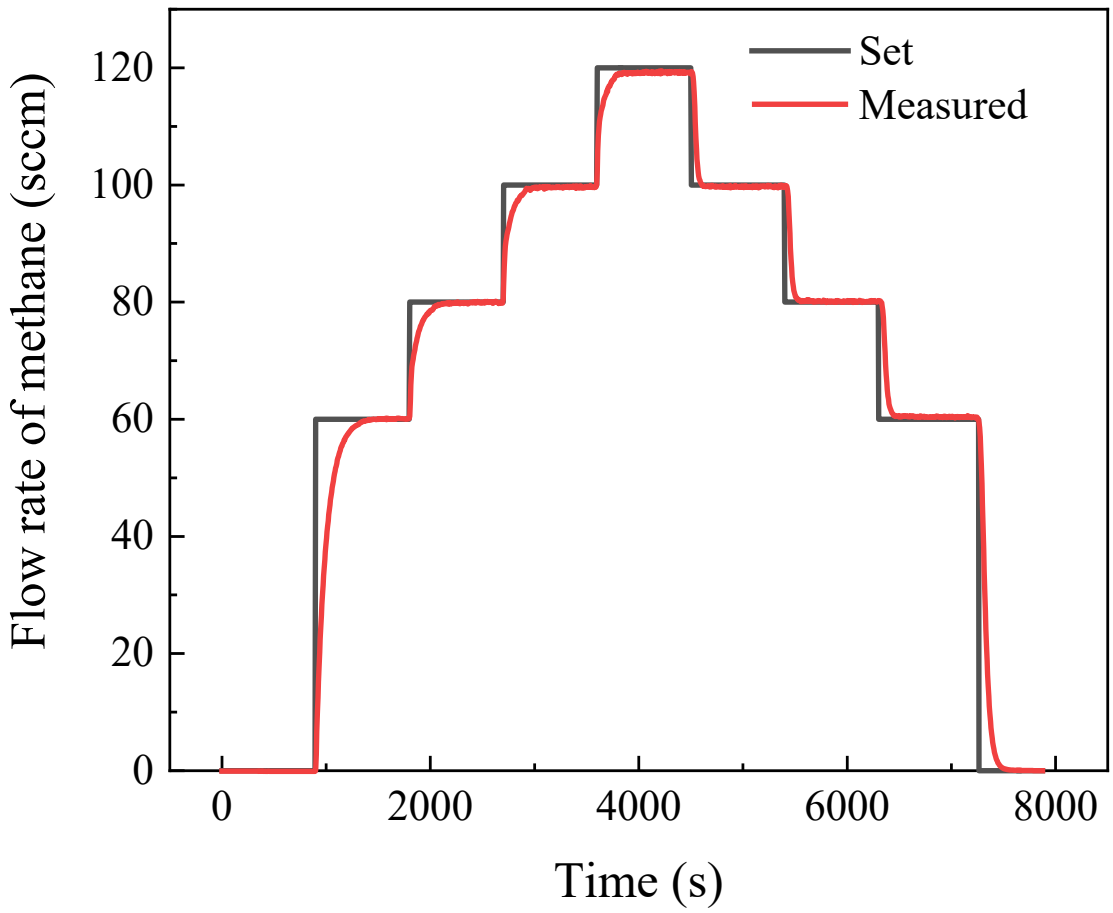

Fig. S13. Comparison between the set and measured values of the methane flow rates for baseline measurements. Methane is introduced into the reactor with step changes in flow rate (0-60-80-100-120-100-80-60-0 mL min^{-1}, STP). No methane reforming reaction occurs in the reactor in the absence of the Ni catalyst.

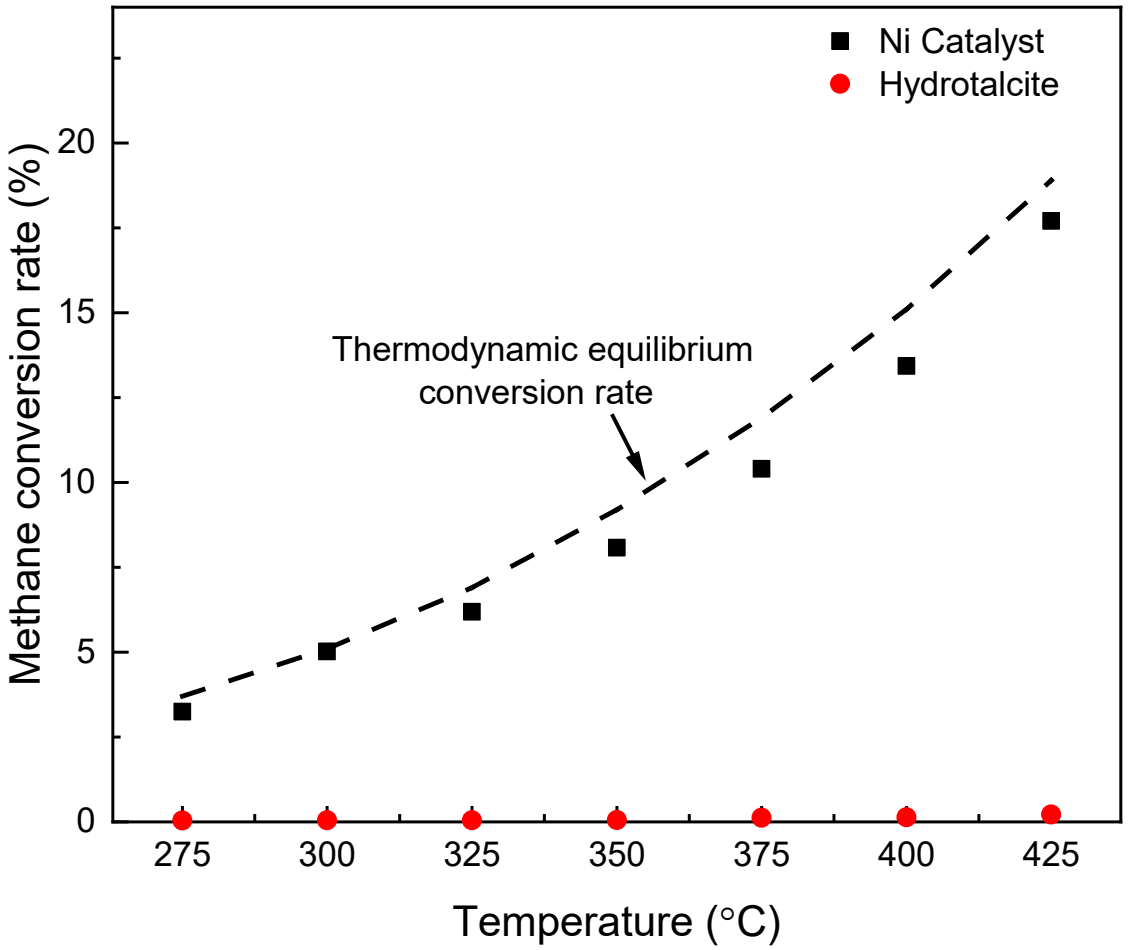

Fig. S14. Results of reference experiments for methane conversion rate with Ni catalyst or hydrotalcite sorbent fixed bed in the temperature range of 275°C to 425°C. Methane flow rate was set to the same gas hourly space velocity (GHSV) as that of sequential separation-driven SMR reaction. Only one material, i.e., Ni catalyst or hydrotalcite, is loaded in the reactor at a time.

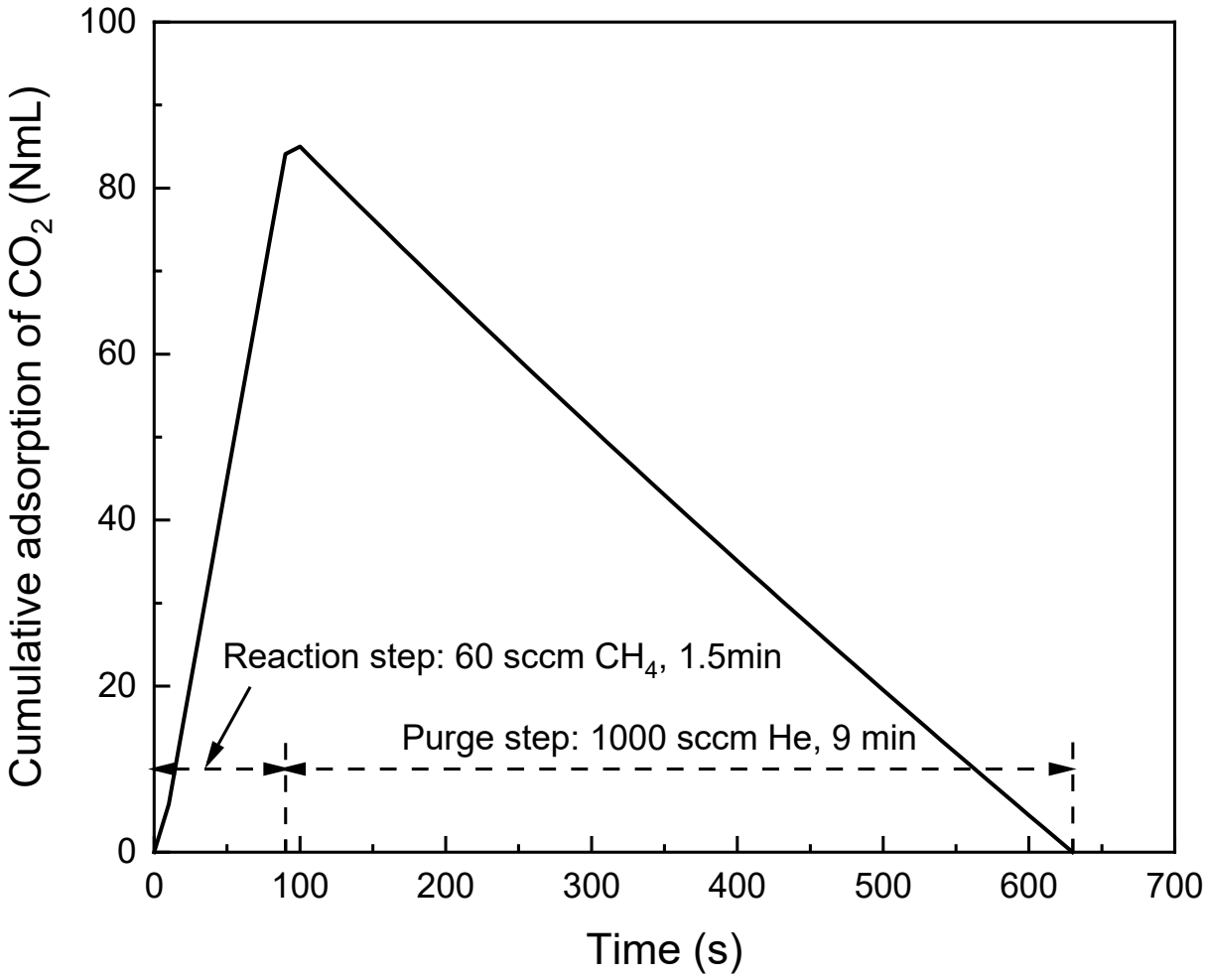

Fig. S15. Simulation results of the cumulative CO_2 adsorption of hydrotalcite in one cycle. The hydrogen separation pressure of vacuum pump is 2000 Pa. The reaction temperature and pressure are 400°C and 10^5 Pa, respectively. The inlet methane flow rate is 60 mL min^{-1} (STP) and the steam-to-methane ratio is 4. In one cycle, the periods of H_2 and CO_2 separation are 1.5 min and 9.0 min, respectively.

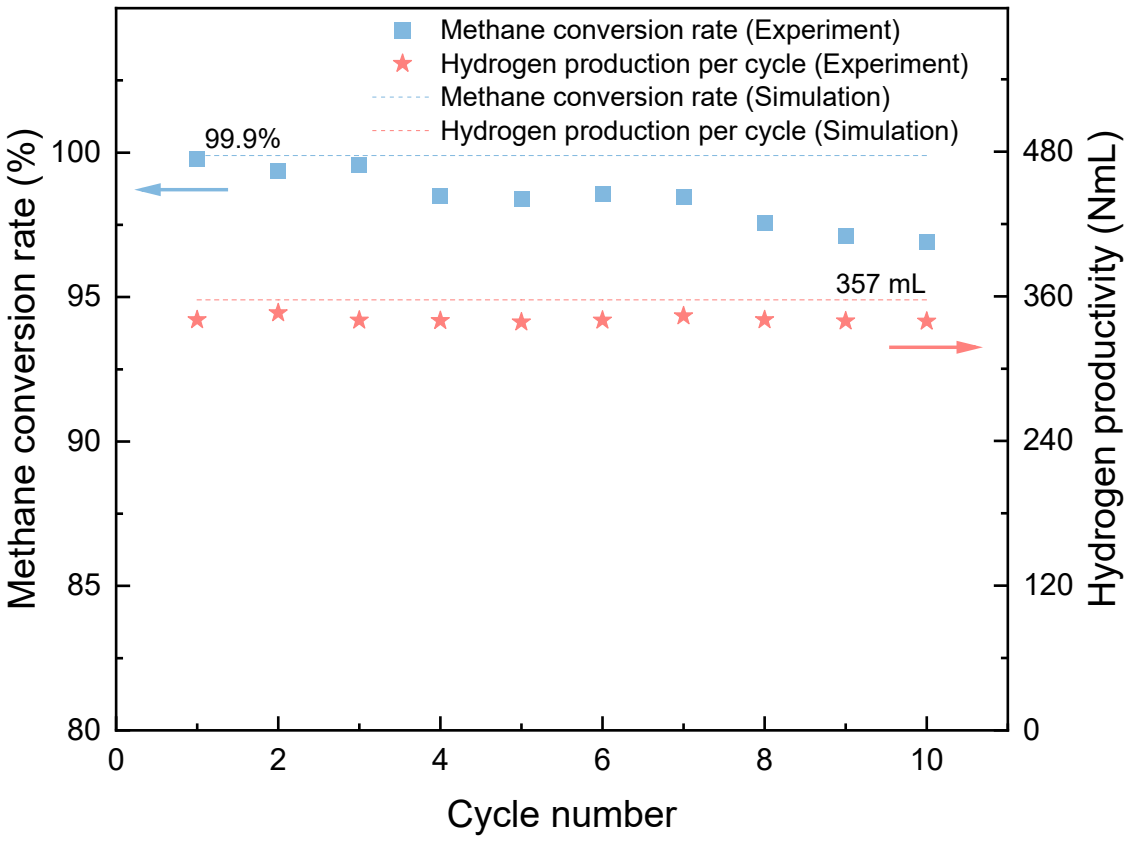

Fig. S16. Comparison of experimental and simulated CH_4 conversion rate and H_2 productivity for 10 consecutive cycles. The reaction temperature and pressure are 400°C and 10^5 Pa, respectively. The inlet methane flow rate is 60 mL min^{-1} (STP) and the steam-to-methane ratio is 4. In each cycle, the periods of H_2 and CO_2 separation are 1.5 min and 9.0 min, respectively.

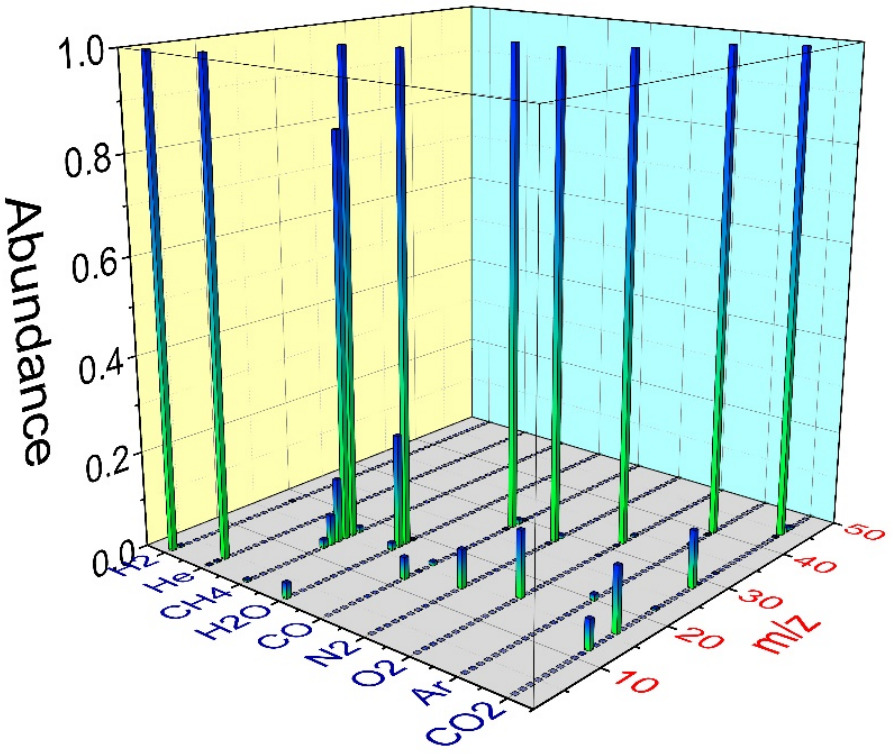

Fig. S17. Mass spectrometer calibration by the ECSA® method for characteristic spectrum of all calibrated gases (Ar, CH_4, CO_2, CO, H_2, He, N_2, O_2 and H_2O) in the experiment. Detailed values of characteristic spectrum and relative sensitivity are shown in Table S22.

Supplementary Tables

Table S1. Conditions for sequential separation-driven SMR experiments.

	Temperature (°C)	Pressure (Pa)	Time (min)	CH_4 (NmL min^{-1})	Steam (NmL min^{-1})	He (NmL min^{-1})	H_2 separation pressure (Pa)
Reaction	400	1×10^5	1.5	60	240	0	2000
Dwell	400	1×10^5	1	0	0	80	2000
Purge	400	1×10^5	9	0	0	1000	No H_2 separation

Table S2. Conditions for long-term durability experiments of sequential separation-driven SMR cycles.

	Temperature (°C)	Pressure (Pa)	Time (min)	CH_4 (NmL min^{-1})	Steam (NmL min^{-1})	He (NmL min^{-1})	H_2 separation pressure (Pa)
Reaction	400	1×10^5	1	100	100	0	5000
Dwell	400	1×10^5	1	0	100	0	5000
Purge	400	1×10^5	2	0	100	1000	No H_2 separation

Note: Steam is continuously fed into the reactor, and steam-to-methane ratio is 4:1.

Table S3. Solar radiation intensity distribution in the heat collecting range of solar trough mirror.

	-0.2 m	0 m	+0.2 m
+1.0 m	166.6 W/m^2	160.4 W/m^2	166.8 W/m^2
+0.5 m	165.6 W/m^2	143.6 W/m^2	149.8 W/m^2
0 m	184.0 W/m^2	180.0 W/m^2	140.0 W/m^2
-0.5 m	151.8 W/m^2	164.0 W/m^2	172.5 W/m^2
-1.0 m	157.3 W/m^2	146.5 W/m^2	152.1 W/m^2

Table S4. Temperature distribution in the sequential separation-driven SMR reactor integrated with parabolic trough solar collector receiver tube.

Thermocouple	-0.2 m	0 m	+0.2 m
# 1	400.5ºC	397.6ºC	395.5ºC
# 2	402.0ºC	401.1ºC	396.2ºC
# 3	403.5ºC	401.5ºC	396.5ºC
# 4	404.2ºC	402.0ºC	396.7ºC
# 5	401.3ºC	400.7ºC	396.6ºC

Table S5. Conditions for sequential separation-driven SMR cycling experiments with solar reactor.

	Temperature (°C)	Pressure (Pa)	Time (min)	CH_4 (NmL min^{-1})	Steam (NmL min^{-1})	He (NmL min^{-1})	H_2 separation pressure (Pa)
Reaction	400	1×10^5	1	100	400	0	2000
Dwell	400	1×10^5	3	0	0	80	2000
Purge	400	1×10^5	2	0	0	1000	No H_2 separation

Table S6. Comparison of energy consumption between sequential separation-driven SMR and industrial SMR for H_2 production.

Design Parameter	This study	Industrial SMR
Methane consumption, reactant (kg-CH_4 kg^{-1}-H_2)	2.00	2.34 [20]
Methane consumption, heating (kg-CH_4 kg^{-1}-H_2)	0.58	0.91 [20-22]
Total Methane consumption (kg-CH_4 kg^{-1}-H_2)	2.58	3.25
Equivalent energy consumption (MJ kg^{-1}-H_2) *	143.6	180.9
Electricity consumption (MJ kg^{-1}-H_2)	2.90	2.04 [7, 20, 23, 24]

* Calculated by the higher heating value (HHV) of CH_4, i.e., 890.6 kJ mol^{-1}.

Table S7. Calculation of the sequential separation-driven SMR reactor size (for designed H_2 production capacity of 50 Nm^3-H_2 h^{-1} [27]).

Parameters	Value	Parameters	Value
Reactor diameter (mm)	40.00	Number of tubes per row	159.00
Reactor tube length (m)	0.38	Tube bundle spacing / diameter size	1.25-1.4 [18, 22]
Cubic volume of single tube (m^3)	6.08×10^{-4}	Total width of tube (m)	2.99-3.34
Hydrogen production rate per tube (mL min^{-1})	116.67	Column tube length (m)	5.94-6.65
Hydrogen production rate per unit volume (Nm^3 min^{-1} m^{-3})	0.192	Total volume (m^3)	6.75-8.45
Number of reaction tubes	7143	Insulation layer volume (m^3)	15.00-20.00
Assuming the number of rows	60.00	Total volume (including insulation) (m^3)	21.75-28.45

Table S8. Comparison of H_2 production cost of sequential separation-driven SMR system with that of industrial SMR with CO_2 capture.

Cost Item	Sequential separation-driven SMR	Industrial SMR
Capital cost ($ kg^{-1}-H_2)	0.43	0.47
O&M phases ($ kg^{-1}-H_2)	0.29	0.25
Feedstock cost ($ kg^{-1}-H_2)	0.41	0.52
LCOH ($ kg^{-1}-H_2)	1.13	1.24

Table S9. Summary of total cost breakdown of sequential separation-driven SMR reactor for the designed H_2 production capacity of 30 ton-H_2 /day.

Component	Material / device	Weight (kg)	Unit Price ($ kg^{-1})	Value ($\times 10^3$ $)	Ref.
Reactor tubing	316L steel	4.03×10^5	3.94	1585.34	[28]
H_2 separation	Pd-Ag Pd	163.83	32025.40	5246.79	[29]
	membrane Ag	49.6	844.80	41.91	[30]
CO_2 sorbent	Li_4SiO_4	2.60×10^5	5.00	1301.41	[31]
SMR catalyst	Ni (40 wt%) / MgO-Al_2O_3	6.96×10^4	9.27	644.59	[32, 33]
	Total	—	—	8820.03	

Table S10. Detailed total cost breakdown of sequential separation-driven reactor for a H_2 production plant with designed capacity 30 ton -H_2 /day, in support of Table S9.

Project	Value	Project	Value
Number of filled sections	6	Volume ratio of palladium to silver	2.88 [34]
Length of each catalyst section	8 mm	Volume of palladium per Pd-Ag membrane	0.00681 cm^3
Length of each lithium silicate section	5.53 mm	Volume of silver per Pd-Ag membrane tube	0.00237 cm^3
Reactor tube length	81.2 mm	Total amount of palladium	163.83 kg
Hydrogen production rate	116.67 mL min^{-1}	Total amount of silver	49.60 kg
Hydrogen production each reactor tube	0.015 kg day^{-1}	Amount of catalyst per reactor tube	34.8 g
Designed hydrogen production per day	30 ton day^{-1}	Amount of lithium silicate per reactor tube	130.2 g
Number of reactors	1999087	Amount of 316L steel per reactor tube	210.43 g
Diameter of each Pd-Ag membrane tube	1.2 cm	Total amount of catalyst	6.96×10^4 kg
Length of each Pd-Ag membrane tube	8.12 cm	Total amount of lithium silicate	2.60×10^5 kg
Thickness of each Pd-Ag membrane tube	3 μm	Total amount of 316L steel	4.03×10^5 kg
Volume per Pd-Ag membrane tube	0.00918 cm^3		

Table S11. Composition and cost breakdown of sequential separation-driven SMR system for the analysis of LCOH (designed H_2 production capacity of 30 ton-H_2 /day).

Item	Value ($\times 10^3$ \$)	Ref.
Direct investment cost (Capital cost, I_t)		
Water supply system	106.1	[20]
Main feed system	270.1	[20]
Boiler	720.0	[20]
Superheater	144.0	[20]
Desulfurization absorption bed	158.2	[20]
Combustion system	76.7	[20]
Sequential separation-driven SMR reactor	8820.0	Calculated by Table S9
Desulfurization preheater	81.4	[20]
Air feed system	92.0	[20]
Reforming cooler	783.8	[20]
Condenser	826.7	[20]
Condenser air supply system	17.3	[20]
Water purification system	819.5	[20]
Integral support	463.8	[20]
Control system	841.8	[20]
System assembly	4832.1	[20]
Miscellaneous	2047.9	[20]
Subtotal, I_t (direct)	21101	
Indirect investment cost (Capital cost, I_t)		
Site preparation (2% of direct investment)	422.0	Calculated by proportion based on the direct investment section
Design and construction (taking 10% of direct investment)	2110.1	
Project emergency (taking 15% of direct investment)	3165.2	

License fee (taking 5% of direct investment)	1055.1	
Subtotal, I_t (indirect)	6752.5	
Operation and maintenance cost (O&M cost, M_t)		
Rent ($/year)	74.2	[20]
Production maintenance and repairs (6% of direct investment) ($/year)	1266.1	[20]
Commercial electricity ($/year)	1669.7	Calculated by Table S6
Subtotal, M_t ($/year)	3010.0	
Feedstock cost, F_t		
Industrial natural gas ($/year)	4346.9	Calculated by Table S6
Subtotal, F_t ($/year)	4346.9	

Notes: Design operation life of the plant is 20 years.

Table S12. Composition and cost breakdown of industrial SMR system with CO_2 capture for the analysis of LCOH (designed H_2 production capacity of 30 ton-H_2 /day)

Project	Value (10^3 $)	Ref.
Direct investment cost (Capital cost, I_t)		
Water supply system	106.1	[20]
Main feed system	270.1	[20]
Boiler	720.0	[20]
Superheater	144.0	[20]
Desulfurization absorption bed	158.2	[20]
Combustion system	76.7	[20]
Reforming system	4744.5	[20]
Water gas conversion unit	3938.8	[20]
PSA unit	1562.4	[20]
Desulfurization preheater	81.4	[20]
Air feed system	92.0	[20]
Reforming cooler	783.8	[20]
Condenser	826.7	[20]
Condenser air supply system	17.3	[20]
CO_2 Sequestration systems	135.6	[20]
Water purification system	819.5	[20]
Integral support	463.8	[20]
Control system	841.8	[20]
System assembly	4832.1	[20]
Miscellaneous	2047.9	[20]
Subtotal, I_t (direct)	22662.7	
Indirect investment cost (Capital cost, I_t)		
Site preparation (2% of direct investment)	453.3	Calculated by
Design and construction (taking 10% of direct	2266.3	proportion

investment)		based on the
Project emergency (taking 15% of direct investment)	3399.4	direct
License fee (taking 5% of direct investment)	2266.3	investment
Subtotal, I_t (indirect)	8385.2	section
Operation and maintenance cost (O&M cost, M_t)		
Rent ($/year)	74.2	[20]
Production maintenance and repairs (6% of direct investment) ($/year)	1359.8	[20]
Commercial electricity ($/year)	1162.5	[20]
Subtotal, M_t ($/year)	2596.5	
Feedstock cost, F_t		
Industrial natural gas ($/year)	5475.7	[20]
Subtotal, F_t ($/year)	5475.7	

Note: Design operation life of the plant is 20 years.

Table S13. Experimental instruments and key parameters.

Instruments	Model	Parameter range	Accuracy
Tubular electric heating furnace	SKGL-1200HL	≤ 1150°C	—
Pressure meter	Y100	0–0.6 MPa	2.5%
Mass flow controller (MFC) of CH_4	CS200-A	0–200 NmL min^{-1}	± 1.0% S.P.
MFC of Ar	CS200-A	0–100 NmL min^{-1}	± 1.0% S.P.
Constant flow pump	P230II	0.001–9.999 mL min^{-1}	Accuracy: ≤ ± 0.3% Stability: RS ≤ 0.1%
Evaporator	SPG-AT01	Flow rate: 0–3 L min^{-1} Temperature: ambient temperature – 300°C	—
Gas pipeline	Diameter 1/8"	—	—
Mass spectrometer	Omnistar GSD 320	—	—

Table S14. Conditions for reference experiments.

	Temperature (°C)	Pressure (Pa)	Sample mass (g)	CH_4 flow rate (NmL min^{-1})	Steam flow rate (NmL min^{-1})
Catalyst	275, 300, 325, 350, 375, 400, 425	1×10^5	3.5	10	40
Hydrotalcite			1.95	10	40

Note: The same gas hourly space velocity (GHSV) as that in sequential separation-driven SMR reaction was applied in reference experiments. The reference experiments involved no separation of H_2.

Table S15. Parameters of noble metal catalyst and hydrotalcite.

	Sample mass (g)	Particle diameter (mm)
Catalyst	39.98 (1 wt% Ru)	1.25
Hydrotalcite	144.08	1.25–2.0

Table S16. Conditions for noble metal catalyst (1 wt% Ru) experiments.

	T (°C)	P (Pa)	Time (min)	CH_4 (NmL min^{-1})	Steam (NmL min^{-1})	He (NmL min^{-1})
Reaction	250–400	1×10^5	1	10	40	0
Dwell	250–400	1×10^5	1.5	0	40	0
Purge	250–400	1×10^5	2	0	40	1000

Note: H_2 separation pressure is 2000 Pa for the reaction and dwell steps (no H_2 separation for the purge step). All flow rates are under standard temperature and pressure conditions.

Table S17. Conditions for adsorption-desorption cycling experiment of the hydrotalcite sorbent.

	Temperature (°C)	Pressure (Pa)	Sample mass (mg)	Duration (min)	CO_2 flow rate (NmL min^{-1})	He flow rate (NmL min^{-1})
CO_2 adsorption	400	1×10^5	3	30	40	60
CO_2 desorption				30	0	100

Table S18. Key parameters of the numerical model.

Key parameters	Value
T (°C)	400
P_{tot} (Pa)	10^5
P_{in} (Pa)	2000
$m_{catalyst}$ (g)	35
$m_{sorbent}$ (g)	130
$V_{catalyst}$ (mL)	30
$V_{sorbent}$ (mL)	200
Sets of catalyst-sorbent combination	6

Table S19. Stoichiometric coefficients of components in the reforming reactions (for Eq. S4).

σ_{ij}		*i*				
		1	2	3	4	5
j	1	-1	-1	+3	+1	0
	2	0	-1	+1	-1	+1
	3	-1	-2	+4	0	+1

Note: The subscript *i* represents gas-phase species *i* (*i*= 1, 2, 3, 4 and 5 corresponding to the species of CH_4, H_2O, H_2, CO and CO_2); the subscript *j* represents the reactions *j* (*j*= 1, 2 and 3 corresponding to Eq.s S8-10).

Table S20. Kinetic parameters of the Ni-based catalyst for SMR.

Parameters	Value	Units
k_1	$3.711\times10^{17}\,\mathrm{e}^{\frac{-240.1\mathrm{kJ\ mol^{-1}}}{RT}}$	(mol $Pa^{0.5}$ kg_{cat}^{-1} s)
k_2	$5.431\mathrm{e}^{\frac{-67.13\mathrm{kJ\ mol^{-1}}}{RT}}$	(mol $Pa^{0.5}$ kg_{cat}^{-1} s)
k_3	$8.960\times10^{16}\,\mathrm{e}^{\frac{-243.9\mathrm{kJ\ mol^{-1}}}{RT}}$	(mol $Pa^{0.5}$ kg_{cat}^{-1} s)
K_{H_2}	$6.120\times10^{-14}\,\mathrm{e}^{\frac{82.90\mathrm{kJ\ mol^{-1}}}{RT}}$	Pa^{-1}
K_{CH_4}	$6.650\times10^{-9}\,\mathrm{e}^{\frac{38.28\mathrm{kJ\ mol^{-1}}}{RT}}$	Pa^{-1}
K_{CO}	$8.230\times10^{-10}\,\mathrm{e}^{\frac{70.65\mathrm{kJ\ mol^{-1}}}{RT}}$	Pa^{-1}
K_{H_2O}	$1.770\times10^{5}\,\mathrm{e}^{\frac{-88.68\mathrm{kJ\ mol^{-1}}}{RT}}$	—
$K_{eq,1}$	$1.198\times10^{23}\,\mathrm{e}^{\frac{-26830\mathrm{K}}{T}}$	Pa^2
$K_{eq,2}$	$1.767\times10^{-2}\,\mathrm{e}^{\frac{4400\mathrm{K}}{T}}$	—
$K_{eq,3}$	$K_{eq,1}K_{eq,2}$	Pa^2
A_{1f}	$\frac{0.74SA}{q_{AS}\sqrt{2\pi M_g RT}}$	kg mol^{-1} s^{-1}
E_{1f}^0	4.90×10^4	J mol^{-1}
α	7.00×10^4	J mol^{-1}
c	1	—
A_{1b}	2.68×10^1	s^{-1}
E_{1b}^0	6.00×10^4	J mol^{-1}
β	8.50×10^4	J mol^{-1}
A_{2f}	2.01×10^6	kg mol^{-1} s^{-1}

E_{2f}	1.00×10^{5}	J mol^{-1}
A_{2b}	4.54×10^{3}	s^{-1}
E_{2b}	6.50×10^{4}	J mol^{-1}
A_{3f}	3.73×10^{2}	kg mol^{-1} s^{-1}
E_{3f}	6.00×10^{4}	J mol^{-1}
A_{3b}	3.95	s^{-1}
E_{3b}	5.80×10^{4}	J mol^{-1}
SA	2.10×10^{4}	kg m^2 mol^{-1} s^{-2}
q_{total}	4.704	mol kg^{-1}
x_K	1.091	—
$q_{A,0}$	0	—
$q_{B,0}$	0	—
$q_{C,0}$	1.8	—
q_{AS}	$0.79\times(q_D+q_E)$	mol kg^{-1}

Table S21. Parameters of the solar-to-hydrogen efficiency analysis.

Parameters	Values	Unit
Maximum thermochemical efficiency	73.2	%
Chemical energy output	252.6	kJ mol^{-1}
Theoretical separation work ($W_{penalty}$)	27.2	kJ mol^{-1}
Carnot efficiency at 400℃ ($\eta_{th\text{-}ele}$)	55.7	%
Thermal energy input for separation	48.9	kJ mol^{-1}
Enthalpy change of reaction	164.7	kJ mol^{-1}
Steam preheating energy	57.2	kJ mol^{-1}
Methane preheating energy	17.2	kJ mol^{-1}
Solar-to-hydrogen efficiency in indirectly heated solar sequential separation-driven SMR	46.5	%
Chemical energy output	255.0	kJ mol^{-1}
H_2 separation work by electrochemical pump	78.9	kJ mol^{-1}-CH_4
CO_2 separation work (inert gas regeneration)	11.8	kJ mol^{-1}
PV conversion efficiency ($\eta_{sol\text{-}ele}$)	30.0	%
Solar energy input for separation	302.2	kJ mol^{-1}
Solar energy input for reaction	197.4	kJ mol^{-1}
Solar energy input for preheating	47.6	kJ mol^{-1}
Solar-to-hydrogen efficiency in directly heated solar sequential separation-driven SMR	3.4	%
Chemical energy output (95% conversion)	242.2	kJ mol^{-1}
Measured direct normal irradiance	160.0	W m^{-2}
Measured solar energy input	6580.2	kJ mol^{-1}

Steam preheating energy	243.5	kJ mol^{-1}
PV conversion efficiency ($\eta_{sol\text{-}ele}$)	30.0	%
Vacuum pump efficiency (η_{pump})	30.9	%
Solar energy input for H_2 separation	299.2	kJ mol^{-1}
Solar energy input for CO_2 separation (inert gas regeneration)	37.4	kJ mol^{-1}

Table S22. Characteristic spectrum and relative sensitivity of calibrated gases in this study by the ECSA® method.

gas	m/z														relative
	2	4	12	13	14	15	16	17	18	20	28	32	40	44	sensitivity
H_2	1.000														0.594
He	0.002	1.000													2.320
CH_4	0.005		0.019	0.064	0.135	0.842	1.000	0.012							0.849
H_2O	0.033						0.016	0.238	1.000						1.238
CO			0.046				0.009				1.000				1.096
N_2					0.082						1.000				1.201
O_2							0.139					1.000			1.742
Ar										0.013			1.000		1.000
CO_2			0.062				0.135				0.120	0.001		1.000	1.475

Table S23. The percentage by weight of each element in the SMR reforming catalyst in three states (support the Fig. S6).

Element	Percentage by weight (%)		
	Initial states	Before-reaction states	Post-6000-cycle states
Ni	48.86	48.85	45.63
C	5.67	6.45	10.03
Mg	4.29	3.82	3.55
Al	13.57	18.31	18.70
O	27.62	22.97	22.08

Supplementary References

1. J. Jin, Y. Hao and H. G. Jin, *Appl. Energy*, 2019, **235**, 1266-1276.
2. gPROMS, Progress systems enterprise limited, UK, 2006.
3. C. Sereno and A. Rodrigues, *Gas Sep. Purif.*, 1993, **7**, 167-174.
4. N. Wakao and T. Funazkri, *Chem. Eng. Sci.*, 1978, **33**, 1375-1384.
5. J. G. Xu and G. F. Froment, *AIChE J.*, 1989, **35**, 88-96.
6. L. Roses, G. Manzolini and S. Campanari, *Int. J. Hydrogen Energy*, 2010, **35**, 12668-12679.
7. H. S. Wang, M. K. Liu, H. Kong and Y. Hao, *Appl. Therm. Eng.*, 2019, **152**, 925-936.
8. B. D. Morreale, M. V. Ciocco, B. H. Howard, R. P. Killmeyer, A. V. Cugini and R. M. Enick, *J. Membr. Sci.*, 2004, **241**, 219-224.
9. H. Tong and Y. Matsumura, *Catal. Today*, 2006, **111**, 147-152.
10. H. S. Wang, Y. Hao and H. Kong, *Int. J. Energy Res.*, 2015, **39**, 1790-1799.
11. Y. Zheng, Y. Shi, S. Li, Y. Yang and N. Cai, *Int. J. Hydrogen Energy*, 2014, **39**, 3771-3779.
12. X. Zhu, Y. Shi, S. Li and N. Cai, *Appl. Energy*, 2018, **229**, 1061-1071.
13. M. T. Gresh, *Compressor Performance:Aerodynamics for the User*, Elsevier, Amsterdam, 2018.
14. D. Marxer, P. Furler, M. Takacs and A. Steinfeld, *Energ. Environ. Sci.*, 2017, **10**, 1142-1149.
15. L. A. Weinstein, Loomis, J., Bhatia, B., Bierman, D. M., Wang, E. N., Chen, G., *Chem. Rev.*, 2015, **115**, 12797-12838.
16. Y. Men, X. Liu and T. Zhang, *Appl. Therm. Eng.*, 2021, **182**, 115715.
17. B. D. Ehrhart, C. L. Muhich, I. Al-Shankiti and A. W. Weimer, *Int. J. Hydrogen Energy*, 2016, **41**, 19881-19893.
18. M. De Falco, Nardella, P., Marrelli, L., Di Paola, L., Basile, A., Gallucci, F., *Chem. Eng. J.*, 2008, **138**, 442-451.
19. H. Xia and K. Wei, *Thermochim. Acta*, 2015, **602**, 15-21.

20. National Renewable Energy Laboratory (NREL), Current Central Hydrogen Production from Natural Gas without CO_2 Sequestration, version 3, 2018.
21. J. C. Molburg and R. D. Doctor, presented in part at the 20th Annual International Pittsburgh Coal Conference, Pittsburgh PA, 2003.
22. B. Zohuri, *Compact Heat Exchangers Design for the Process Industry. In: Compact Heat Exchangers: Selection, Application, Design and Evaluation.*, Springer International Publishing, 2017.
23. Y. Chen, Y. Wang, H. Xu and G. Xiong, *J. Membr. Sci.*, 2008, **322**, 453-459.
24. G. Shahani and C. Kandziora, Linde Engineering, 2014, 1001013.
25. I. Mohsin, T. A. Al-Attas, K. Z. Sumon, J. Bergerson, S. McCoy and M. G. Kibria, *Cell Rep. Phys. Sci.*, 2020, **1**, 100104.
26. HSC Chemistry 5.11, Outokumpu Research Oy, Pori, Finland, A. Roine, 2001-2002.
27. S. T. Wismann, Engbaek, J. S., Vendelbo, S. B., Bendixen, F. B., Eriksen, W. L., Aasberg-Petersen, K., Frandsen, C., Chorkendorff, I., Mortensen, P. M., *Science*, 2019, **364**, 756-759.
28. https://www.yole9.com/bxg/price/316.html, (accessed Mar 24, 2021).
29. https://www.apmex.com/palladium-price, (accessed Aug 6, 2018).
30. https://www.apmex.com/silver-price, (accessed Jan 18, 2022).
31. Y. Yang, W. Liu, Y. Hu, J. Sun, X. Tong, Q. Li and Z. Zhou, *Chem. Eng. J.*, 2019, **374**, 328-337.
32. https://markets.businessinsider.com/commodities/nickel-price, (accessed Jan 17, 2022).
33. https://www.lme.com/Metals/Non-ferrous/LME-Alumina#Trading+day+summary, (accessed Jan 25, 2022).
34. J. Melendez, E. Fernandez, F. Gallucci, M. van Sint Annaland, P. L. Arias and D. A. Pacheco Tanaka, *J. Membr. Sci.*, 2017, **528**, 12-23.